INTERNATIONAL GEOLOGY REVIEW
https://doi.org/10.1080/00206814.2019.1671237

ARTICLE

Flexural bending curvature and yield zone of subducting plates

Fan Zhang[a,b], Jian Lin[a,c] and Zhiyuan Zhou[a,b]

[a]Key Laboratory of Ocean and Marginal Sea Geology, South China Sea Institute of Oceanology, Chinese Academy of Sciences, Guangzhou, China; [b]Innovation Academy of South China Sea Ecology and Environmental Engineering, Chinese Academy of Sciences, Guangzhou, China; [c]Department of Geology and Geophysics, Woods Hole Oceanographic Institution, Woods Hole, MA, USA

ABSTRACT
We quantify flexural deformation of subducting oceanic plates at a global array of 15 ocean trenches, using a new approach of modelling spatial variations in flexural bending shape and curvature. The investigated trenches are chosen to represent a diverse range of subducting plate age of 24–150 Ma, including the Middle America, Peru, Chile, West and East Aleutian, Sumatra, North and South Philippine, Tonga, Kermadec, Kuril, Japan, Izu-Bonin, and South and North Mariana. The studied trenches show systematic intra- and inter-trench variability in the calculated flexural bending curvature, stress distribution, extensional brittle yield zone, and effective elastic plate thickness T_e of the subducting plates. We find that subducting plate age is a critical factor controlling the bending curvature and the corresponding extensional yield zone. The width, depth, and area of the extensional yield zone are all calculated to increase systematically with the subducting plate age. The newly-developed curvature analysis can yield continuously varying apparent $T_e(x)$ from the trench axis to outer rise. The calculated extensional yield zones from the curvature analysis are in general consistent with the observed normal faulting earthquakes of magnitude≥6.0 at the 15 global trenches. Our analyses also reveal that the five deepest regions of the global trenches, i.e. the Challenger, Horizon, Serena, and Scholl Deeps and Galathea Depth, are associated with relatively large flexural bending and calculated yield zones comparing to their respective adjacent trench segments. The Serena and Challenger Deeps of the S. Mariana trench are calculated to have the largest flexural bending among the five deeps.

ARTICLE HISTORY
Received 16 June 2019
Accepted 19 September 2019

KEYWORDS
Subducting plate; flexural bending; curvature analysis; stress variations; extensional brittle yield zone

1. Introduction

Flexural bending causes extensional brittle yielding at the shallow part and compressional ductile deformation at the lower part of a subducting plate (e.g. Garcia-Castellanos *et al*. 2000; Watts 2001; Zhang *et al*. 2014; Hunter and Watts 2016; Zhang et al 2018a, 2018b, 2018c). The significant extensional yielding of the upper subducting plate is reflected by the observation of both pervasive seafloor normal faults (Grevemeyer *et al*. 2007; Zhou *et al*. 2015; Zhou and Lin 2018) and normal faulting earthquakes at the outer-rise regions (Ranero *et al*. 2003, 2005; Bry and White 2007; Obana *et al*. 2012; Fujie *et al*. 2013; Naliboff *et al*. 2013; Boston *et al*. 2014; Craig *et al*. 2014; Emry *et al*. 2014). Furthermore, normal faults may provide conduits for fluids to enter the crust and upper mantle (Ranero and Sallares 2004; Rupke *et al*. 2004; Grevemeyer *et al*. 2007; Faccenda *et al*. 2009; Contreras-Reyes *et al*. 2013). The subsequent serpentinization of the upper mantle peridotite may further weaken the lithosphere (Escartin *et al*. 2001). Thus, understanding the key factors controlling the interaction of plate bending, normal faulting, and extensional yielding is of great significance to study the dynamics of the subduction zones (Billen and Gurnis 2005; Supak et al. 2006; Arredondo and Billen 2012; Naliboff *et al*. 2013; Zhou and Lin 2018; Zhou *et al*. 2018).

A key issue in modelling vertical deflection is the ability to invert for the spatial variations in the effective elastic thickness T_e and other bending variables from the trench axis to the outer rise. Previous studies have modelled T_e as 3–4 segments of piecewise constant T_e values (Contreras-Reyes and Osses 2010) or two segments of piecewise constant T_e and a transition point distance X_r (Zhang *et al*. 2014, 2018a). On the other hand, Hunter and Watts (2016) used the plate bending model to approximate linear reduction in T_e from the outer rise to the trench axis. However, in reality, the reduction in T_e is neither abrupt nor linear, and thus innovative methods to solve for continuously varying T_e are highly desired. To achieve this goal, Zhou and Lin (2018) modelled the development of discrete normal faults in an elastoplastic plate and obtained profiles of continuously varying T_e (x) across the Mariana Trench. This approach,

CONTACT Jian Lin jlin@whoi.edu Department of Geology & Geophysics, Woods Hole Oceanographic Institution, Woods Hole, MA 02543, USA; Zhiyuan Zhou zyzhou@scsio.ac.cn South China Sea Institute of Oceanology, Chinese Academy of Sciences, Guangzhou 510301, China
This article has been republished with minor changes. These changes do not impact the academic content of the article.

however, depends on the availability of high-resolution multibeam bathymetry to determine normal fault distribution. Since multibeam bathymetry is still lacking for many parts of the global trenches, we need to continue seeking innovative approaches to obtain continuously varying $T_e\,(x)$ solutions.

Estimation of yield zone in the subducting plate is crucial for evaluating outer-rise normal faulting region and water content carried into the subduction zones. The bending curvature of the subducting plate increases towards the trench axis, causing an extensional brittle yield zone in the upper plate, and resulting in a significant decrease in effective elastic plate thickness. Turcotte et al. (1978) and Goetze and Evans (1979) used perfectly-plastic and brittle-elastic-ductile rheology to predict this brittle failure region, respectively. The extensional yield zone at the Mariana Trench has also been predicted by elastoplastic model (Zhou and Lin 2018), which is shown to be consistent with the location of observed outer-rise normal faulting earthquakes. However, for most of the global subduction zones, the yield zone prediction is still lacking.

In this study, we use a new flexural curvature approach to investigate the spatial extent of brittle yield zone of a global array of 15 trenches, and compare the results to the observed normal faulting seismicity. The curvature is also used to yield continuously varying *apparent* $T_e(x)$ from the trench axis to outer rise. The investigated trenches include the Middle America, Peru, Chile, W. and E. Aleutian, Sumatra, N. and S. Philippine, Tonga, Kermadec, Kuril, Japan, Izu-Bonin, and S. and N. Mariana Trenches. Results of the analyses reveal strong age dependence of flexural bending and extensional yield zone. We also illustrate that the five deepest regions of the global trenches are associated with relatively large flexural bending and extensional yield zone comparing to their respective adjacent trench segments.

2. Data analysis

Our overall investigative strategy is to analyse flexural bending of an array of 15 global trench regions (Figure 1), obtain models of stress distribution and extensional yield zone, and compare the results with observed normal faulting distribution. The subducting plate age varies significantly among the 15 global trenches from 24 to 150 Ma (Table 2). The studied trenches can be categorized in four plate age groups: *Group 1* is associated with the youngest subducting plate (average 24 Ma) of the Middle America Trench. *Group 2* includes several trenches of moderate subducting plate age (average 43–59 Ma), including the Peru, Chile, W. and E. Aleutian, Sumatra, and N. Philippine. *Group 3* is associated with significantly older subducting plates (average 96–112 Ma), including the S. Philippine, Kermadec, Tonga, and Kuril. *Group 4* is associated with

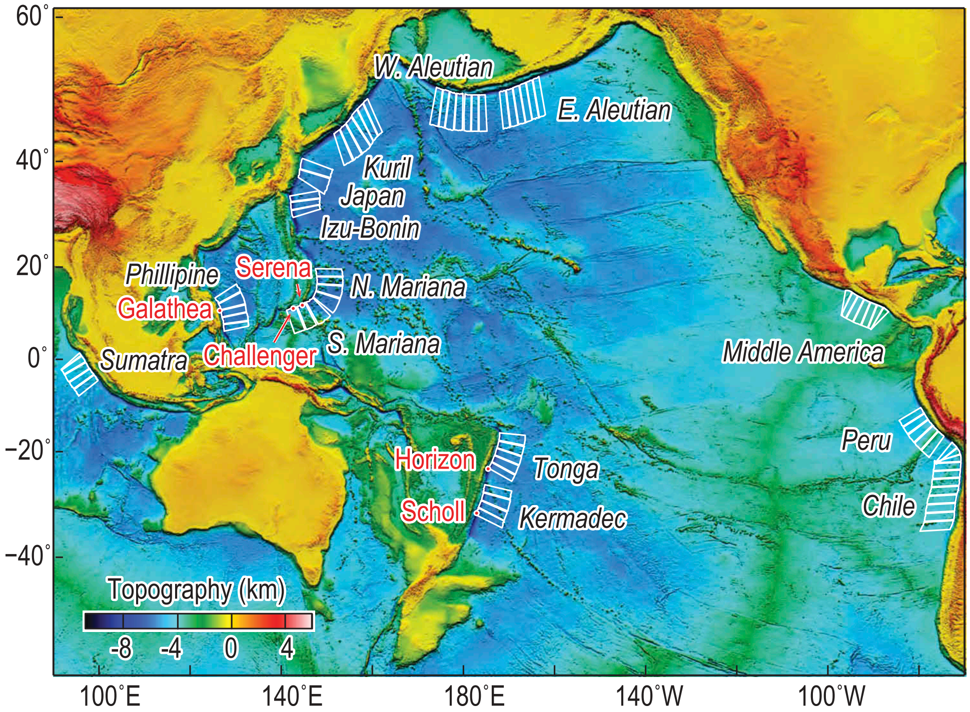

Figure 1. Topography of the global ocean basins showing study areas. White boxes mark the profile locations of the 15 investigated trenches. A total of 73 profile sections are analysed among the 15 global trenches, including the Sumatra, N. and S. Philippine, Tonga–Kermadec, S. and N. Mariana, Izu-Bonin, Japan, Kuril, W. and E. Aleutian, Middle America, Peru, and Chile. The locations of the Challenger, Horizon, Serena, and Scholl Deeps, and Galathea Depth are shown by red dots.

Table 1. Variables used in flexural modelling.

Symbol	Variables	Value	Unit
E	Young's modulus	$7x10^{10}$	Pa
g	Acceleration due to gravity	9.81	m s^{-2}
v	Poisson's ratio	0.25	
ρ_w	Seawater density	1,030	kg m^{-3}
ρ_s	Sediment density	2,000	kg m^{-3}
ρ_c	Crust density	2,700	kg m^{-3}
ρ_m	Mantle density	3,300	kg m^{-3}
μ	Friction coefficient	0.6	

Table 2. Key parameters of 15 global trenches from observations and curvature analysis.

Trench name	Age (Ma)	W_0 (km)	X_0 (km)	X_c (km)	T_e^M (km)*	T_e^m (km)	X_r (km)	$S_{\Delta T_e}$ (km^2)	S_{yz} (km^2)	σ_{max-e} (MPa)	σ_{max-c} (MPa)	Y_{max-e} (km)	Y_{max-c} (km)	$H_{elastic}$ (km)
Group 1	**Avg**													
	Min-Max													
Middle America	**24**	**1.9**	**45**	**71**	**34**	**12**	**54**	**1153**	**1290**	**241**	**−454**	**16**	**20**	**4**
	20-25	1.6–2.3	36-63	65-73	32-35	10-16	20-60	1080-1237	1269-1361			15-16		
Group 2														
Peru	**43**	**1.7**	**65**	**85**	**40**	**21**	**60**	**1096**	**1611**	**256**	**−485**	**17**	**26**	**9**
	41-46	1.2–2.3	50-89	71-103	33-44	17-24	40-65	686-1518	1299-2010			14-19		
Chile	**46**	**2.9**	**55**	**95**	**42**	**18**	**70**	**1559**	**1901**	**271**	**−498**	**19**	**27**	**8**
	36-53	2.0–3.7	47-73	80-108	25-45	15-25	45-80	709-1930	1185-2290			11-21		
W. Aleutian	**53**	**2.6**	**53**	**109**	**47**	**21**	**85**	**1932**	**2195**	**316**	**−507**	**21**	**28**	**7**
	49-57	1.5–3.5	33-72	76-126	44-50	20-32	50-105	1200-2488	1639-2555			19-22		
Sumatra	**54**	**1.0**	**60**	**86**	**51**	**24**	**47**	**1285**	**1818**	**316**	**−364**	**22**	**32**	**10**
	44-68	0.8–1.3	29-106	59-113	47-55	21-32	10-65	1015-1560	1616-2102			19-24		
E. Aleutian	**58**	**1.6**	**38**	**90**	**46**	**22**	**62**	**1331**	**1941**	**301**	**−559**	**20**	**28**	**8**
	56-62	1.4–1.7	32-47	72-93	40-50	18-28	45-70	1018-1630	1627-2117			18-22		
N. Philippine	**59**	**1.1**	**50**	**69**	**44**	**20**	**45**	**912**	**1792**	**286**	**−560**	**19**	**28**	**9**
	59-59	1.1–1.1	50-50	69-69	44-44	20-20	45-45	912-912	1792-1792			19-19		
Group 3														
S. Philippine	**96**	**2.1**	**40**	**79**	**47**	**23**	**48**	**1067**	**1968**	**331**	**−876**	**22**	**28**	**6**
	85-105	0.9–2.7	35-60	68-91	40-50	16-25	40-50	787-1423	1643-2199			19-24		
Kermadec	**96**	**3.9**	**62**	**104**	**49**	**21**	**77**	**1598**	**2411**	**316**	**−725**	**22**	**32**	**10**
	89-102	3.5–4.2	53-69	92-107	46-50	16-22	60-80	1280-1752	2112-2444			20-23		
Tonga	**100**	**3.8**	**85**	**94**	**47**	**22**	**63**	**1378**	**2342**	**316**	**−853**	**21**	**29**	**8**
	93-106	3.5–4.1	75-100	86-101	43-50	15-23	45-67	1161-1547	2083-2587			20-23		
Kuril	**112**	**3.6**	**60**	**123**	**45**	**27**	**72**	**1207**	**2452**	**301**	**−885**	**20**	**30**	**10**
	107-116	2.8–4.7	48-68	91-126	39-50	20-29	60-85	735-1657	1804-2733			17-23		
Group 4														
Japan	**132**	**2.4**	**64**	**114**	**50**	**34**	**68**	**958**	**2610**	**306**	**−742**	**22**	**36**	**14**
	131-133	2.3–2.6	61-70	105-124	48-52	31-35	60-85	951-963	2441-2692			21-22		
Izu-Bonin	**136**	**4.5**	**84**	**131**	**53**	**33**	**92**	**1574**	**3193**	**346**	**−803**	**23**	**35**	**12**
	134-139	4.4–4.6	71-99	129-134	51-54	18-35	89-100	1507-1609	2980-3308			23-23		
S. Mariana	**149**	**3.5**	**72**	**117**	**52**	**36**	**68**	**982**	**2575**	**344**	**−1033**	**22**	**32**	**10**
	148-152	3.2–3.6	66-84	109-126	46-55	22-38	10-110	862-1220	2481-2670			21-23		
N. Mariana	**150**	**2.6**	**75**	**124**	**50**	**29**	**62**	**1165**	**2726**	**331**	**−784**	**22**	**36**	**14**
	147-151	2.1–2.9	71-80	106-133	48-55	28-32	55-100	953-1462	2594-2728			20-24		

* T_e^M values are from inversion of five flexural bending parameters assuming two segments of piecewise constant T_e values.

the oldest subducting plates (average 132–150 Ma), including the Japan, Izu-Bonin, and S. and N. Mariana.

To investigate the common characteristics of the deepest trench regions, we also analyse flexural bending of the five deepest regions in the world with trench depth greater than 10 km (Figures 1, B1 and B2(a)), including the Challenger (trench depth of 10.9 km) and Serena (10.7 km) Deeps of the Mariana Trench, Horizon (10.8 km) and Scholl (10.0 km) Deeps of the Tonga–Kermadec Trench, and the Galathea Depth (10.1 km) of the Philippine Trench.

The following section describes five key steps of analysis involving both data analysis and theoretical modelling: (1) Analysis of non-isostatic topography; (2) Inversion of bending parameters assuming two segments of piecewise constant T_e; (3) Calculation of flexural bending curvature; (4) Calculation of extensional yield zone; and (5) Calculation of spatially varying apparent $T_e(x)$.

2.1. Step 1: analysis of non-isostatic topography

To better reveal the flexural bending shape of a subducting plate, we first calculate 'non-isostatic' topography by removing the following predictable components from the observed bathymetry (data sources: http://topex.ucsd.edu/WWW_html/mar_topo.html, v18.1, Smith and Sandwell 1997): (1) Sediment loading (https://www.ngdc.noaa.gov/mgg/sedthick/sedthick.html; Divins 2003); (2) Airy-isostatic topography calculated from gravity-derived crustal thickness model (Zhang *et al*. 2014, 2018a); and (3) Age-related thermal subsidence (Müller *et al*. 2008; Turcotte and Schubert 2014). The resultant 'non-Airy-isostatic topography' reflects stress-supported flexure, as well as deviations from the above assumptions (Zhang *et al*. 2014, 2018a). Details of non-isostatic topography analysis are described in Appendix A. The non-Airy-isostatic topography is then converted to the vertical deflection $w(x)$ relative to the far-field reference seafloor depth ($w= 0$) of the subducting plate.

We extract 730 across-trench profiles of the non-isostatic topography at the 15 studied regions (Figure 1). The spacing between two adjacent profiles is 15 km and the length of each profile is 600 km. Every 10 profiles are grouped as a profile section and smoothed, yielding a total of 73 sections (Figure 3). We also extract additional profiles at the five deepest trench regions (Figure 1) with the non-isostatic topography profiles shown in Figure B2(b).

2.2. Step 2: inversion of bending parameters assuming two segments of piecewise constant T_e

Our approach is to start with the simplest two-segment model of piecewise constant T_e values, and then progress towards the solution of continuously varying apparent $T_e(x)$. In all models, we conduct thin-plate analysis assuming an elastic plate overlying inviscid asthenosphere.

In the first set of modelling, we assume an end-member model of two segments of piecewise constant T_e values and conduct the analysis using the algorithm developed by Contreras-Reyes and Osses (2010) and modified by Zhang *et al*. (2014). For each profile section, we obtain five bending parameters that best fit the interpreted deformation (Figure 2(e)): Axial vertical loading ($-V_0$), axial bending moment ($-M_0$), maximum (unfaulted) effective elastic thickness before the plate is deformed (T_e^M), minimum effective plate thickness after faulting (T_e^m), and a break point distance (X_r) at the transition of the two T_e values. The detailed procedure of inverting bending parameters of the two-T_e models is described in Appendix B. The constant parameters used in this study are listed in Table 1. We obtain 73 sets of bending parameters for the 15 studied trenches and five sets of parameters for the deepest regions (Appendix B). We then calculate the regionally averaged values of bending parameters for the 15 global trenches (Table B1) and the five deepest trench regions (Table B2).

2.3. Step 3: calculation of flexural bending curvature

For each profile, we first calculate the flexural bending curvature $\kappa(x) = d^2w/dx^2$ as a function of distance from the trench axis (Figure 2(b)). The flexural bending shape $w(x)$ we use in calculating the curvature is a synthetical profile of theoretical prediction based on the best-fitting parameters of the two-T_e model for the corresponding profile section. Such a synthetic profile has the major advantage of being much smoother than the actual observed flexural bending profile.

We then further smooth surface slope $dw/dx(x)$ of this synthetical profile by filtering out local spikes (Figure B7). Such additional smoothing helps to ensure that the resultant curvature κ would capture the essential features in the regional variation of the flexural bending shape (Figure 2(b)). Using the above method, curvature solutions are obtained for the 73 profile sections of the 15 studied trenches and for profiles across the five deepest trench regions (Figure 4).

2.4. Step 4: calculation of extensional yield zone

The maximum sustainable deviatoric stress of an elastoplastic plate is constrained by the yield strength envelope (YSE) (e.g. Byerlee 1978; Chen and Morgan 1990; Garcia-Castellanos *et al*. 2000; Hunter and Watts 2016). When the deviatoric stress exceeds the YSE, brittle failure and plastic deformation are predicted to occur in the upper and lower plate, respectively (Figure 2(c)). The maximum sustainable deviatoric stress in the upper plate is determined by maximum shear stress $\Delta\tau = \mu(\sigma_n - P_f)$, where μ is rock frictional coefficient, σ_n normal stress, and P_f pore fluid pressure on fault planes. Meanwhile, the plastic deformation is controlled by the temperature-dependent power-law rheology (Goetze 1978; Goetze and Evans 1979; Kirby 1983; Chen and Morgan, 1990; Hirth and Kohlstedt 2003; Mei et al. 2010). Two experimentally derived mantle flow lows are used in this study, including: (1) the low-temperature plasticity law on the form of $\dot{\varepsilon} = -A\sigma^{\mathrm{n}}\frac{H_0}{RT}\left[(1-\left(\frac{\sigma}{\sigma_p}\right)^p\right]^q$; (2) the power-law creep law on the form of $\dot{\varepsilon} = B\sigma^{\mathrm{n}}\exp(-\frac{E+PV}{RT})$, where $\dot{\varepsilon}$, σ, n, H_0, R, T, σ_{p}, E, P, and V, are the strain rate, differential stress, stress exponent, zero-stress activation enthalpy, gas constant, temperature, Peierls stress, activation energy, pressure, and activation volume, respectively, while A and B are pre-exponential coefficients and p and q are geometry-dependent parameters. The values of the parameters used are listed in Table B3. Between the upper brittle yield zone and the lower

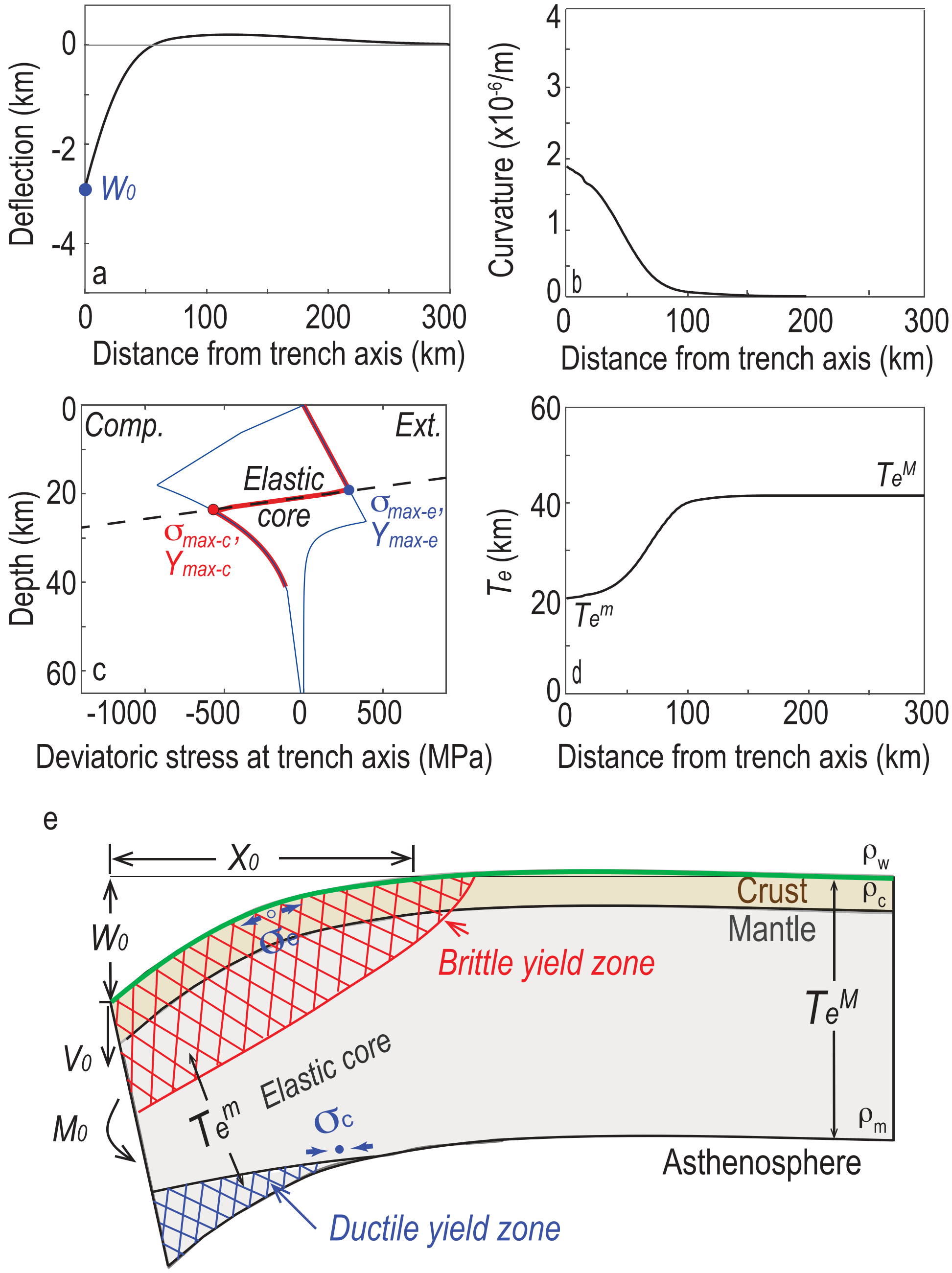

Figure 2. Illustration of key flexural bending variables of an example subducting plate: (a) Flexural bending shape. Deflection of trench axis (w_0) is marked by blue dot. Far-field reference seafloor depth is marked by grey line; (b) flexural bending curvature; (c) deviatoric stress at trench axis; and (d) effective elastic thickness. (e) Schematic model of a subducting plate. The flexural bending shape is shown by the green curve. Key bending parameters include the following: -V_0 the axial vertical loading; -M_0 the axial bending moment; X_0 the location where vertical deformation $w = 0$; T_e^M and T_e^m the effective elastic plate thickness seaward of the outer-rise region and at the trench axis, respectively. The upper and lower parts of the plate near the trench are associated with brittle yield zone (red stripes) and ductile yield zone (blue stripes), respectively. Modified from Zhang *et al.* (2018a).

layer of plastic deformation, an elastic core is expected to be sandwiched at the central depth (Figure 2(c)); the depth-slope of the deviatoric stress in this elastic core is constrained by the curvature κ of the smoothed flexural bending shape as discussed above.

We further calculate the deviatoric stress (Figure 2(c)) in the elastic core as follows: $\Delta\sigma_{xx}^{elastic} = \frac{E(y-y_n)\kappa}{1-\nu^2}$, where E is Young's modulus, ν Poisson's ratio, y depth, y_n depth of the neutral plane, and κ curvature (Hunter and Watts 2016; Zhang *et al.* 2018a). Then, the brittle yield zone is determined by the maximum deviatoric stress and YSE.

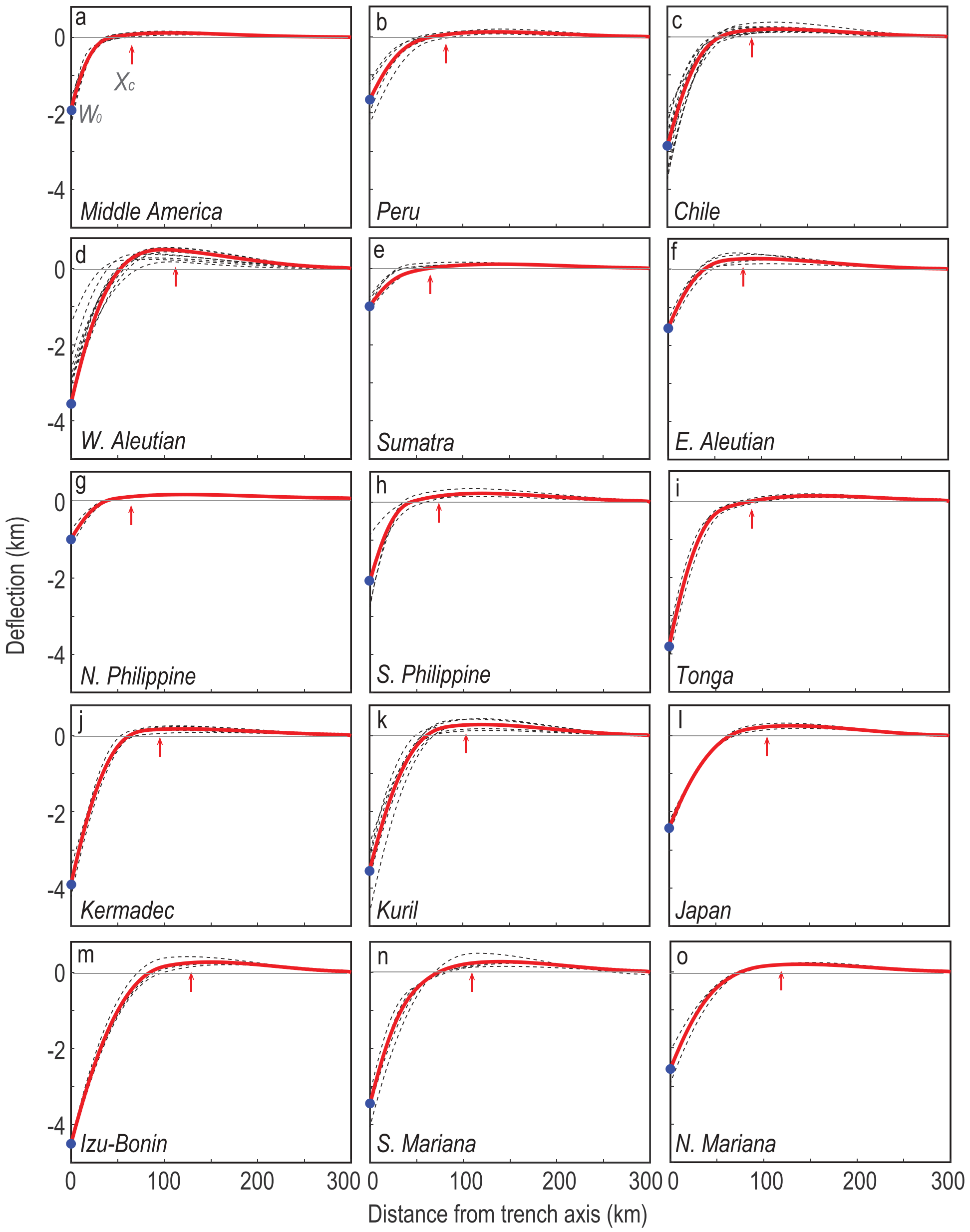

Figure 3. Smoothed flexural bending shapes (w) of 73 profile sections across the 15 studied trenches. For each trench, black dashed thin curves show individual profile sections, while thick red curve shows the averaged profile of the trench. Average deformation of trench axis (w_0) is marked by blue dot. Far-field reference seafloor depth is marked by grey line. Red arrows mark the characteristic distance (X_c) at which the flexural bending curvature decreases to a negligible value (0.1×10^{-6} m^{-1}); values of X_c are from Figure 4.

The deviatoric stresses at the trench axis are calculated for the 15 studied trenches (Figure 5) and the five deepest trench regions (Figure B3). The deviatoric stresses for the entire profile sections are also calculated for the 15 studied trenches (Figure 6) and the deepest trench regions (Figure B4).

2.5. Step 5: calculation of spatially varying apparent $T_e(x)$

The last step is to obtain solution of spatially varying apparent $T_e(x)$ from the above elastoplastic model with yield zone. The plate bending moment $M(x)$ is calculated by integrating the deviatoric stress in the plate and the vertical distance from the neutral plane depth as: $M=\int_0^{T_e}\Delta\sigma_{xx}(y-y_n)dy$, where $\Delta\sigma_{xx}$ is horizontal deviatoric stress in the plate. We calculate the flexural rigidity D from its relationship with curvature and bending moment (Turcotte and Schubert 2014) $M=-D\frac{d^2w}{dx^2}=D\kappa$. We then calculate the effective elastic plate thickness T_e (x) from $T_e=\left[\frac{12(1-\nu^2)D}{E}\right]^{\frac{1}{3}}$, as a function

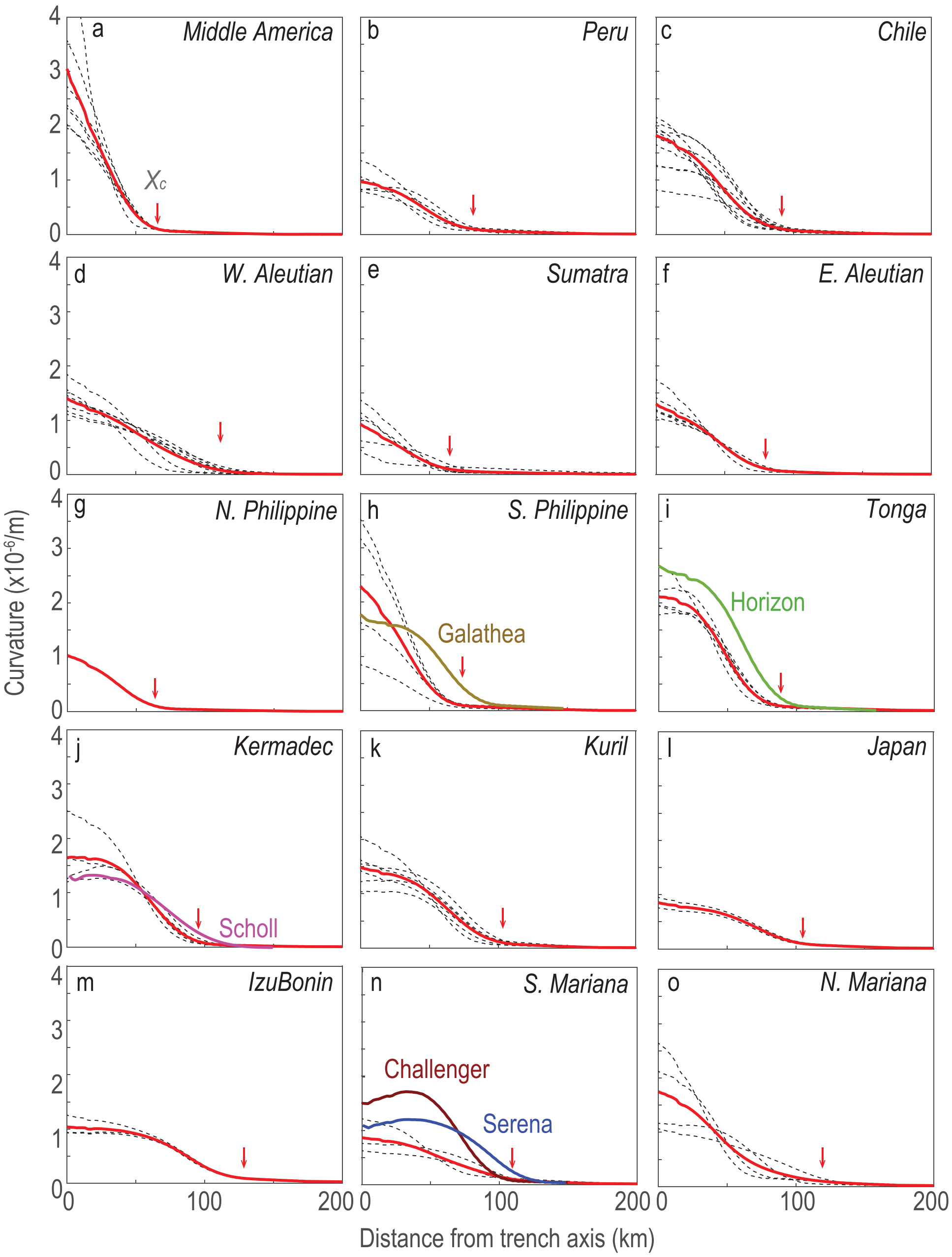

Figure 4. Calculated flexural bending curvature ($k = d^2w/d^2x$) of the studied trenches. For each trench, black dashed thin curves show individual profile sections, while thick red curve shows the averaged profile of the trench. Also shown are the calculated curvatures of the Galathea Depth (brown), and Horizon (green), Scholl (purple), Challenger (marron), and Serena (blue) Deeps. Red arrows mark the characteristic distance (X_c) at which the flexural bending curvature decreases to a negligible value (0.1×10^{-6} m^{-1}).

of distance from the trench axis (Figure 2(d)). Finally, we calculate the T_e reduction area $S_{\Delta Te} = \int_0^{Xr} [Te^M - Te(x)]dx$, which is the integrated amount of T_e reduction along an across-trench profile (Figure 2(d)) (Zhang *et al*. 2018a). In the end-member case of two-T_e bending models, $S_{\Delta Te} = (T_e^M - T_e^m)\ X_r$.

Therefore, the apparent $T_e(x)$ is not a physical plate thickness; instead, it contains combined information of curvature, brittle and ductile yield zones, and elastic core. The solutions of continuously varying apparent $T_e(x)$ are obtained for the studied trenches and the five deepest regions (Figure 7). The T_e reduction areas $S_{\Delta Te}$ are also calculated for both the two-T_e model and the apparent $T_e(x)$ for the studied trenches (Table 2) and the deepest regions (Table 3).

3. Results

We conduct comparative analysis of the studied global trenches and the deepest trench regions, showing systematic variations in flexural bending parameters as detailed below.

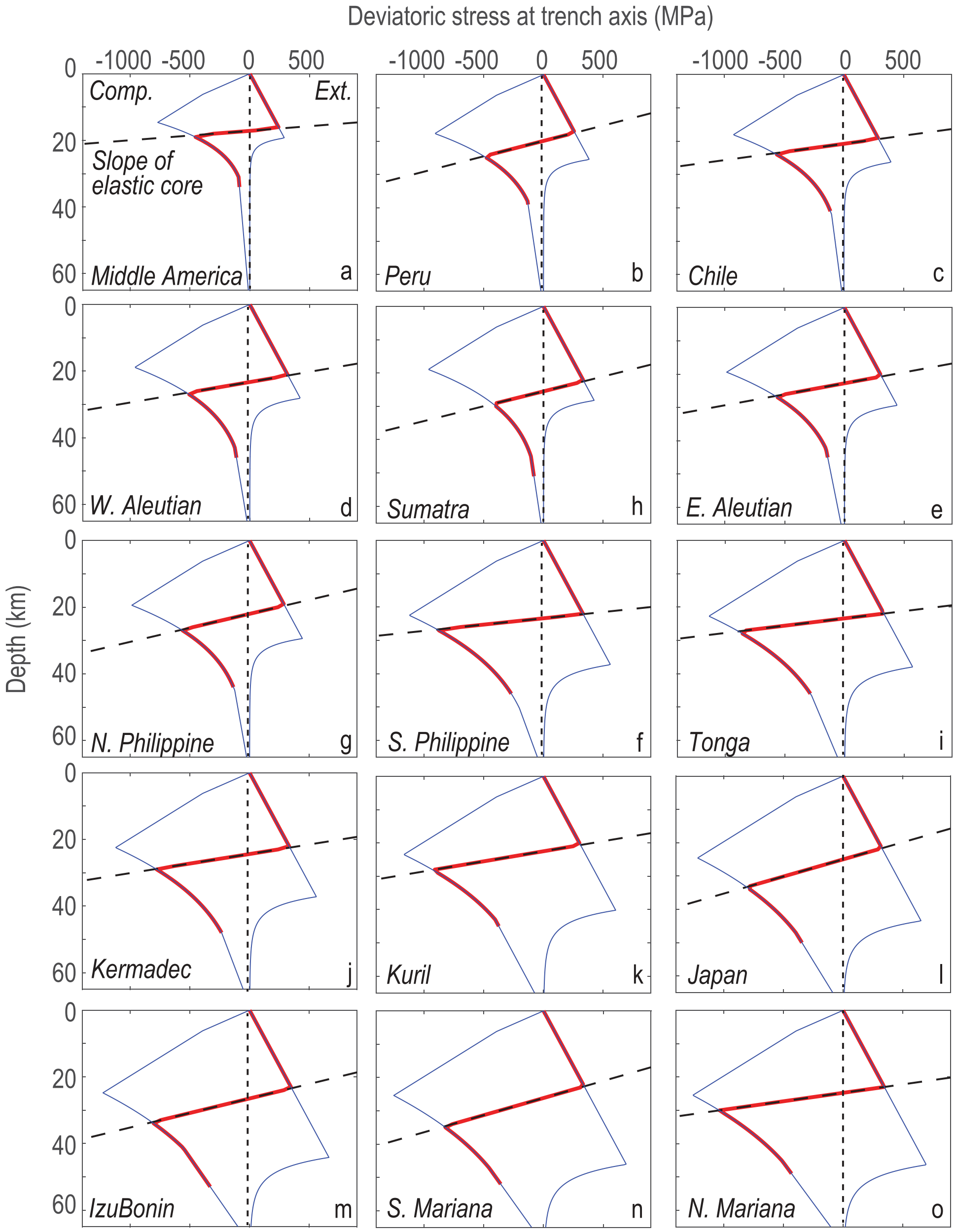

Figure 5. Calculated deviatoric stress as a function of depth at the trench axis. Blue curves mark the yield strength envelope (YSE); black dashed lines mark the slope of the elastic core; red curves mark the calculated deviatoric stress as a function of depth in the plate.

3.1. Variations in flexural bending shape and axial loading

The magnitude of plate flexural bending, as characterized by the trench-averaged value of trench relief W_0, varies greatly among the studied trenches (Figure 3, Table 2), ranging from the relatively small values of Sumatra (1.0 km) and N. Philippine (1.1 km) to the much larger values of Izu-Bonin (4.5 km), Kermadec (3.9 km), and Tonga (3.8 km). The trench width X_0 also varies significantly, ranging from the E. Aleutian (38 km) and S. Philippine (40 km) to Tonga (85 km) and Izu-Bonin (84 km) (Figure 3, Table 2).

All of the five deepest trench regions are associated with relatively large flexural bending: the calculated trench relief W_0 varies from the Serena Deep (5.5 km) to Challenger Deep (5.2 km), Horizon Deep (5.0 km), Galathea Depth (3.8 km), and Scholl Deep (3.7 km) (Figure B2(b), Table 3). The trench width X_0 is also relatively large, ranging from the Challenger Deep (97 km) to Serena Deep (83 km), Galathea Depth (77 km), Horizon Deep (68 km), and Scholl Deep (66 km) (Figure B2(b), Table 3). The corresponding FAA varies from the Challenger Deep (−322 mGal) to the Scholl Deep (−240 mGal) (Figure B2(c)).

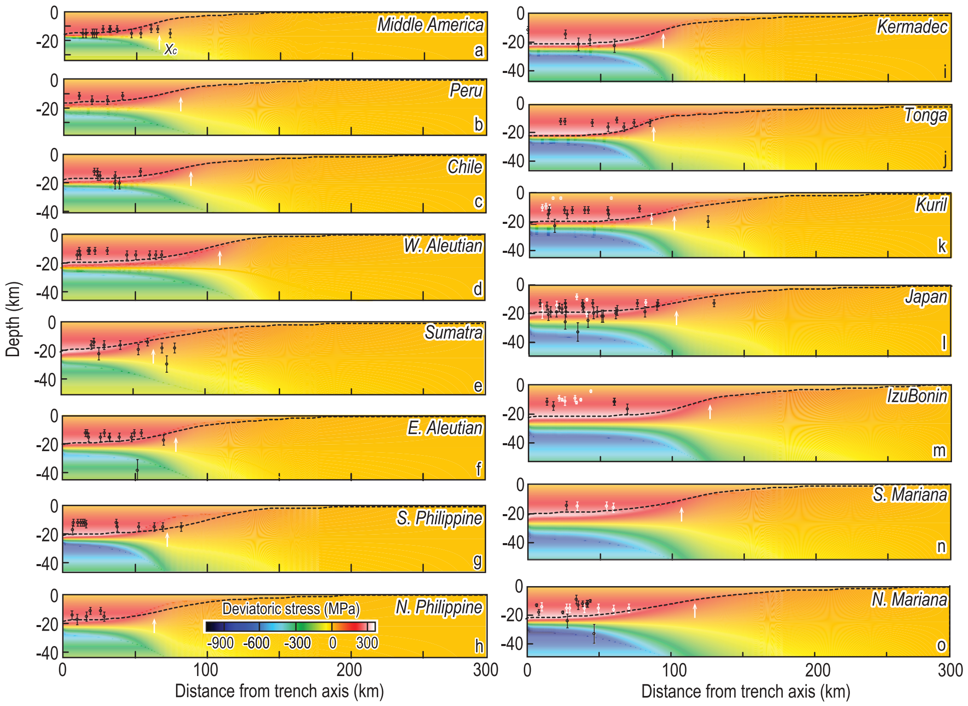

Figure 6. Calculated deviatoric stress in the upper yield zone (red), central elastic core, and lower ductile layer (blue) of subducting plates. For each trench, black dashed curves mark the maximum brittle yield zone depth; black circles mark the normal faulting earthquakes recorded by the GMT database; white circles mark the relocated earthquakes from Emry and Wiens (2015). White arrows mark the characteristic distance (X_c) at which the flexural bending curvature decreases to a negligible value (0.1×10^{-6} m^{-1}); values of X_c are from Figure 4.

The axial loading parameters are obtained from the two-T_e bending model for the studied trenches (Table B1) and deepest regions (Table B2). The calculated trench-averaged axial vertical force $-V_0$ varies from the E. Aleutian (-0.4×10^{12} N/m) to Izu-Bonin (1.77×10^{12} N/m) (Table B1). All of five deepest trench regions are associated with relatively large axial vertical force, ranging from the Galathea Depth (1.2×10^{12} N/m) to the Challenger and Serena Deeps (2.6×10^{12} N/m) (Table B2). The calculated trench-averaged axial bending moment $-M_0$ varies from the Middle America (3.6×10^{16} N) to Izu-Bonin (19.3×10^{16} N) (Table B1), and from the Scholl Deep (1×10^{16} N) to Galathea Depth (11×10^{16} N) (Table B2).

3.2. Variations in flexural bending curvature

We calculate flexural bending curvature for each profile of the studied trenches (Figure 4). The calculated curvatures for most individual profiles reach maximum near the trench axis and decrease with distance from the trench axis. There are significant variations in curvature between individual profiles within a trench. For example, the maximum curvature for individual profiles of the Middle America Trench varies between 2.0 and 6.3×10^{-6} m^{-1} (Figure 4(a)).

The maximum curvature of the trench-averaged profiles varies from the Middle America Trench (3.0×10^{-6} m^{-1}) to S. Mariana Trench (0.8×10^{-6} m^{-1}) (Figure 4). The curvatures of the five deepest trench regions are in general consistent with the averaged curvatures of their corresponding trenches. It is noted, however, curvatures of the Challenger and Serena Deeps are significantly greater than the averaged values of the S. Mariana (Figure 4(n)), indicating that these two local deeps might have greater flexural bending than the adjacent segments.

We also calculate the characteristic distance X_c, at which the trench-averaged curvature decreases to a relatively small reference value of 0.1×10^{-6} m^{-1} (Figure 4, Table 2). The N. Philippine Trench has the smallest value of X_c (69 km), while the Izu-Bonin Trench has the largest value (131 km). The calculated characteristic distance X_c of the studied trenches generally increase with plate age (Figure 8(a)). All of the five deepest trench regions are associated with relatively large values of X_c, ranging from the Serena Deep (136 km) to Scholl Deep (112 km), indicating that these deep regions are associated relatively strong subducting plates.

3.3. Variations in extensional yield zones

Theoretical models of brittle yield zone of a trench can be compared with observed seismicity data and thus provide important insights into the trench processes.

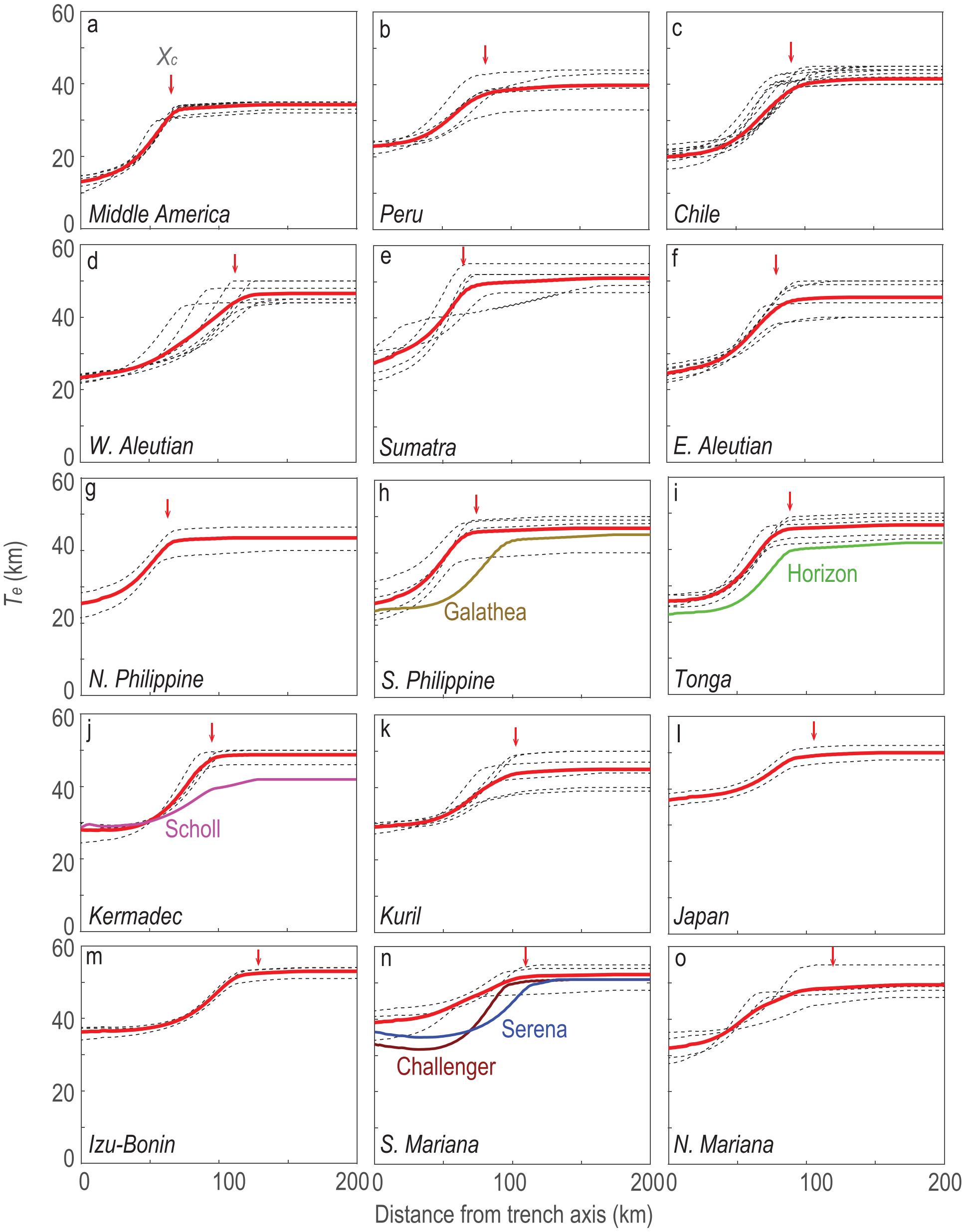

Figure 7. Calculated variations in apparent $T_e(x)$ across the studied trenches. For each trench, black dashed thin curves show individual profile sections, while thick red curve shows the averaged profile of the trench. Red arrows mark the characteristic distance (X_c) at which the flexural bending curvature decreases to a negligible value (0.1×10^{-6} m^{-1}); values of X_c are from Figure 4.

Table 3. Key parameters of five deepest trench regions from observations and curvature analysis.

Deep name	Lon (°)	Lat (°)	Age (Ma)	Depth (km)	W_0 (km)	X_0 (km)	X_c (km)	T_e^{M*} (km)	T_e^m (km)	X_r (km)	$S_{\Delta}T_e$ (km^2)	Dyz (km)	Syz (km^2)	σ_{max-e} (MPa)	σ_{max-c} (MPa)
Challenger	142.59	11.37	149	10.9	5.2	97	123	51	31	89	1507	23	2767	346	−943
Horizon	−174.73	−23.26	89	10.8	5.0	68	120	42	20	67	1411	20	2249	287	−928
Sirena	144.58	12.07	149	10.7	5.5	83	136	51	34	95	1477	22	2793	331	−861
Galathea	126.5	10.9	94	10.1	3.8	77	120	45	22	73	1583	20	2418	301	−678
Scholl	−177.25	−31.9	112	10.0	3.7	66	112	42	29	79	1032	18	2052	271	−883

* T_e^M values are from inversion of five flexural bending parameters assuming two segments of piecewise constant T_e values.

Static deviatoric stress is calculated for each of the trench-averaged profile of the global array of subducting plates at the trench axis (Table 2) and as a function of distance along the profile (Figure 6). At the trench axis of the Middle America Trench, the youngest among the studied trenches, the maximum extensional deviatoric stress (Figure 2(c)) is

$\sigma_{max\text{-}e} = 241$ MPa, which is reached at depth $Y_{max\text{-}e} = 16$ km. Likewise, the maximum compressional deviatoric stress (Figure 2(c)) is $\sigma_{max\text{-}c} = -454$ MPa, which is reached at depth $Y_{max\text{-}c} = 20$ km, together with an elastic core thickness $H_{elastic} = Y_{max\text{-}c} - Y_{max\text{-}e} = 4$ km (Table 2). In comparison, the old subducting plate of the S. Mariana Trench is associated with much greater deviatoric stresses of $\sigma_{max\text{-}e} = 344$ MPa and $\sigma_{max\text{-}c} = -1{,}033$ MPa that occur at greater depths of $Y_{max\text{-}e} = 22$ km and $Y_{max\text{-}c} = 32$ km, respectively, with a thicker elastic core of $H_{elastic} = 10$ km (Table 2).

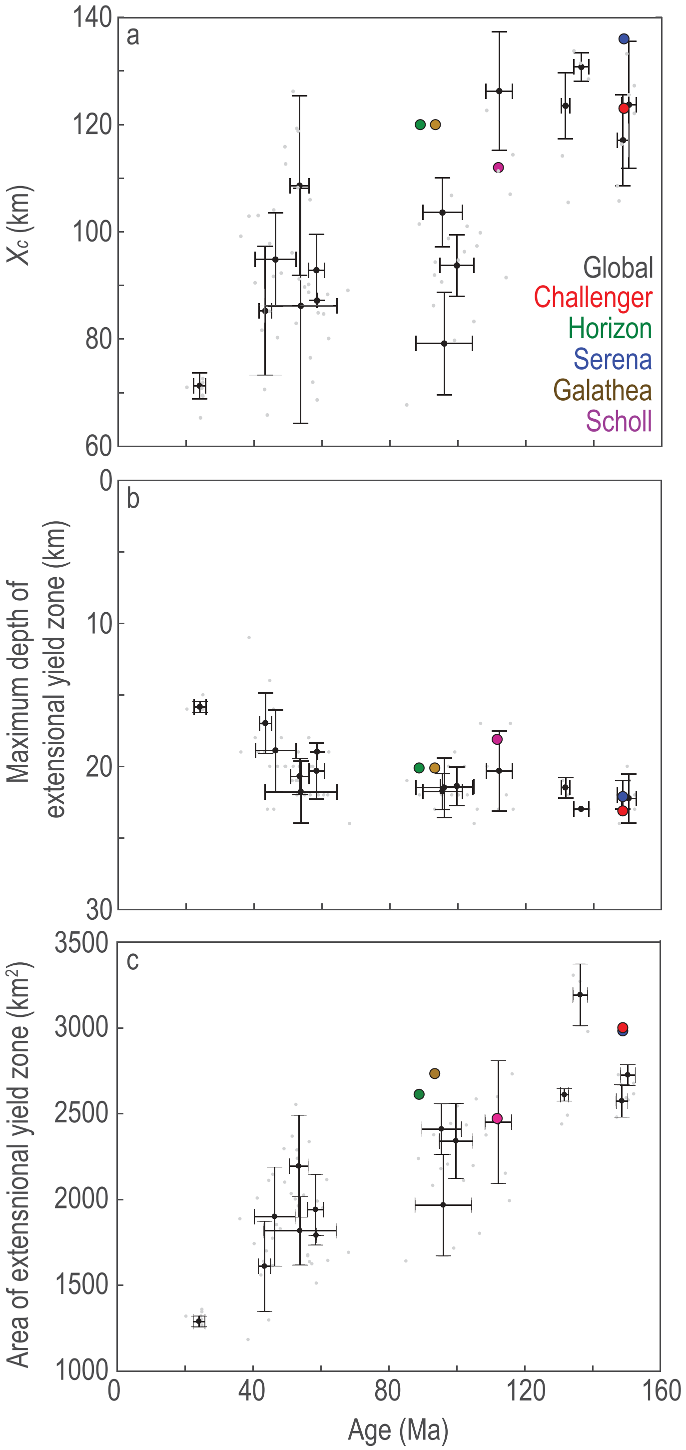

Figure 8. Calculated key bending parameters as a function of subducting plate age: (a) critical distance of the flexural bending curvature; (b) maximum depth of the extensional yield zone in the upper plate; and (c) area of extensional yield zone. Also shown by colour dots are the corresponding values of the Galathea (brown) Depth, and Horizon (green), Scholl (purple), Challenger (red), and Serena (blue) Deeps.

The maximum extensional and compressional deviatoric stresses at the trench axis of the 15 studied trenches are calculated to be in the range of $\sigma_{max\text{-}e}$ = 241 to 346 MPa and $\sigma_{max\text{-}c}$ = −454 to −1,033 MPa, respectively (Table 2). The maximum deviatoric stresses occur at depths of $Y_{max\text{-}e}$ = 16–23 km and $Y_{max\text{-}c}$ = 20–36 km, corresponding to elastic core thickness of $H_{elastic}$ = 4–14 km. The corresponding total yield zone area S_{yz} is in the range of 1,290–3,193 km^2 (Table 2). It is observed that both the extensional yield zone depth $Y_{max\text{-}e}$ (Figure 8(b)) and the total yield zone area S_{yz} (Figure 8(c)) increase with plate age. The deepest trench regions are associated with relatively large extensional yield zone depth $Y_{max\text{-}e}$ of 18–23 km (Figure 8(b)) and relatively large total yield zone area (Table 3).

3.4. *Variations in effective elastic plate thickness T_e*

The effective elastic thickness of the subducting plates is calculated (Figure 7). The trench-averaged T_e^M is calculated from the two-T_e bending models. T_e^m is obtained from the new $T_e(x)$ solution through the curvature analysis (Figure 7). The new $T_e(x)$ solutions also reveal the average reduced T_e trench-ward of the outer-rise region. It is noticed that the transition from T_e^M to T_e^m is not linear and instead has a shape of cosine taper (Figure 7). For the studied trenches, the averaged T_e^M = 34–53 km and T_e^m = 12–36 km, respectively (Figure 7, Table 2), reflecting a maximum reduction in effective elastic thickness of $R = (T_e^M - T_e^m)/T_e^M$ =38%-63%.

Both the T_e^M and T_e^m values are calculated to increase with subducting plate age (Figure 9). The T_e^M by the two-T_e model for the studied trenches are in the range of ~650–850°C isotherms according to the plate cooling model of Parsons and Sclater (1977) (isothermals not shown) or ~600–800°C based on the thermal model of McKenzie *et al*. (2005) (Figure 9). The T_e^m calculated by both the two-T_e model and curvature analysis are all in the range of ~300–500°C isotherms based on the model of Parsons and Sclater (1977) or ~300–450°C based on the model of McKenzie *et al*. (2005) (Figure 9). Hunter and Watts (2016) reached similar conclusions from modelling the FAA, showing that the best-fitting temperature ranges are 342 ±35°C for trench-averaged T_e^m values or 714 ±75°C for T_e^M values, respectively, based on the thermal model of Parsons and Sclater (1977). The trench-averaged T_e reduction area $S_{\Delta Te}$ is in the range of 912–1,932 km^2 for the studied trenches (Table 2).

For the deepest trench regions, the T_e^M is calculated to be in range of 42 km (Horizon and Scholl Deeps) to 51 km (Challenger and Serena Deeps) (Table 3). The T_e^m is calculated to be in range of 10–23 km and 20–34 km, respectively, from the two-T_e bending model (Table B2) and curvature analysis (Table 3). The *Xr* is in range of 60–100 km and 67–95 km, respectively, from the two-T_e model (Table B2) and curvature analysis (Table 3). The calculated T_e reduction area $S_{\Delta Te}$ is in the range of 1,386–2,810 km^2 and 1,032–1,583 km^2, respectively, from the two-T_e model (Table 3) and curvature analysis (Table B2).

4. Discussion

4.1. *Brittle yield zone and normal faulting earthquakes*

To illustrate the relationship between the calculated extensional yield zone at the upper plate and the normal faulting earthquakes, we extract earthquakes with

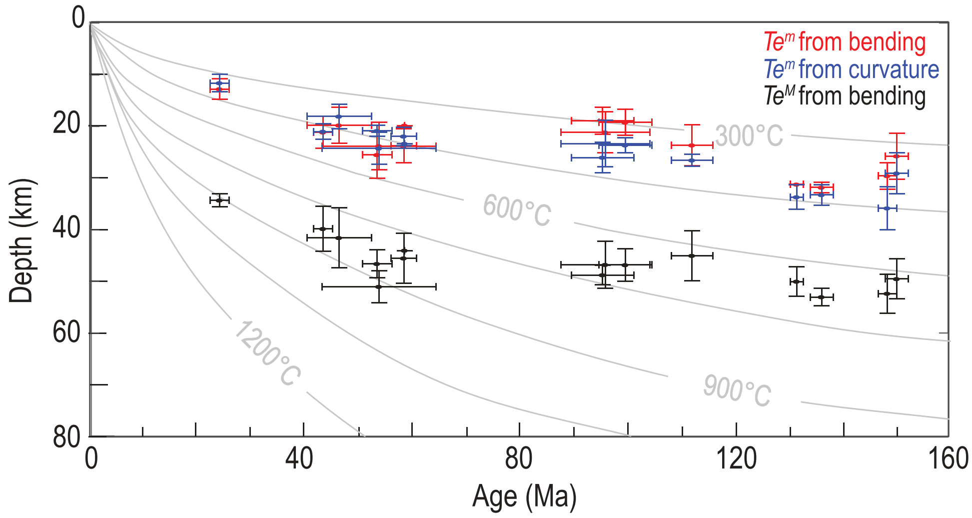

Figure 9. Calculated T_e^M (black dots) and T_e^m (red dots) from the two-T_e model, and T_e^m from the curvature analysis (blue dots), respectively. Grey curves are isotherms from the thermal model of McKenzie *et al*. (2005).

magnitude≥6.0 in the study regions from the global database of moment tensor solutions (http://www.globalcmt.org). Normal faulting earthquakes (rake between −135° and −45°) occurred since 1976 are extracted for these regions. For the Kuril, Japan, Izu-Bonin, S. and N. Mariana Trenches, we also add results of relocated normal faulting earthquakes (Emry and Wiens 2015). Finally, all normal faulting earthquakes are projected to the cross-sections of stress distribution (Figure 6). We found that most normal faulting earthquakes are distributed within the calculated brittle yield zone. Since bending-induced normal faults could provide conduits for fluids to reach the upper mantle and facilitate serpentinization (Yamano and Uyeda 1990; Ranero *et al*. 2003; Grevemeyer *et al*. 2007), the mantle portion of the brittle yield zone could be considered as potential serpentinization zone. Therefore, the trench-averaged potential serpentinization zone might increase with subducting plate age (Figure 8(c)).

4.2 Comparison of results between two-T_e and spatially varying apparent $T_e(x)$ models

The trench-averaged T_e^m of the studied trenches is 12–36 km and 12–32 km (Figure 10(a)), and the break point distance *Xr* is 47–91 km and 36–98 km (Figure 10(b)) from the curvature analysis and two-T_e model, respectively. The calculated average $S_{\Delta Te}$ for the studied trenches is 912–1,932 km^2 and 781–2,163 km^2 (Figure 10(c)) from the curvature analysis and two-T_e bending models, respectively. Values of the break point distance from the two methods also show strong consistency (Figure 10(b)), which indicate that the calculated curvature and wavelength of the bending shape are relatively robust. Both the calculated trench-averaged reduction in T_e and $S_{\Delta Te}$ from two-T_e model are in general consistent with, but show some deviations with, the results from curvature analysis (Figure 10(a,c)). Some discrepancies between the two models are expected since the two-T_e model is a real physical input in the inversion of best-fitting solution, while the apparent $T_e(x)$ from curvature analysis contains combined information of curvature, brittle and ductile yield zones, and elastic core.

If we use the apparent $T_e(x)$ as a physical model to calculate plate flexure, the resultant best-fitting solution of axial loading are expected to differ somewhat from the best-fitting solutions of two-T_e models. In fact, for a given observed profile, the best-fitting solutions of axial loading shall always depend on the shape of $T_e(x)$ used in inversion.

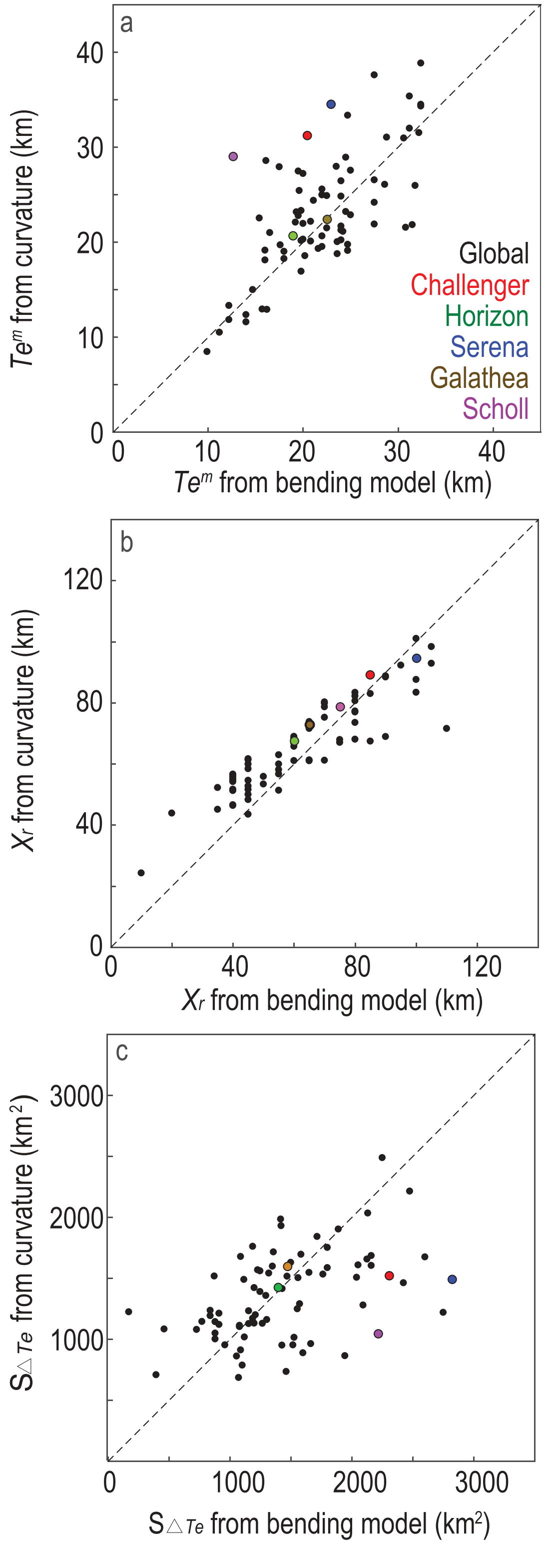

Figure 10. Comparison between results of flexural curvature analysis and two-T_e model: (a) T_e^m, (b) X_r, and (c) $S_{\Delta}T_e$. Black dots correspond to 73 profile sections of the 15 studied trenches. Colour dots mark the results of the five deepest trenches.

5. Conclusions

A detailed analysis of the 15 studied global trenches and five deepest trench regions yield the following key results:

1. Subducting plate age is shown to be an important factor controlling the bending curvature and the corresponding extensional brittle yield zone. The width, depth, and area of the extensional yield zone are calculated to increase with the subducting plate age.
2. The calculated areas of brittle yield zone from the curvature analysis are in general consistent with the distribution of observed normal faulting earthquakes of magnitude≥6.0 in the 15 investigated trenches.
3. The five deepest regions on Earth, i.e. the Challenger, Horizon, Serena, Scholl Deeps and Galathea Depth, are all associated with relatively large flexural bending and calculated yield zones in comparison to their respective adjacent segments. The Serena and Challenger Deeps of the Mariana Trench are associated with the largest flexural bending among the five deeps.

Acknowledgments

We benefited from stimulating discussion with Drs. Hongfeng Yang, Huihui Weng, Yen Joe Tan, and SCSIO Marine Geodynamics Group. We are grateful to editor Robert Stern, reviewer Felipe Orellana-Rovirosa, and the other two anonymous reviewers whose comments have significantly improved the revised manuscript. This work was supported by NSFC Grants (41976064, 41890813, 91628301, U1606401, 41976066, and 41706056), CAS Grants (Y4SL021001, QYZDY-SSW-DQC005, and 133244KYSB20180029), National Key R&D Program of China Grants (2018YFC0309800 and 2018YFC0310100), and China Ocean Mineral Resources R&D Association (DY135-S2-1-04).

Disclosure statement

No potential conflict of interest was reported by the authors.

References

Arredondo, K.M., and Billen, M.I., 2012, Rapid weakening of subducting plates from trench-parallel estimates of flexural rigidity: Physics of the Earth and Planetary Interiors, v. 196, p. 1–13. doi:10.1016/j.pepi.2012.02.007.

Billen, M.I., and Gurnis, M., 2005, Constraints on subducting plate strength within the Kermadec trench: Journal of Geophysical Research, v. 110, p. B05407. doi:10.1029/2004JB003308.

Boston, B., Moore, G.F., Nakamura, Y., and Kodaira, S., 2014, Outer-rise normal fault development and influence on near-trench décollement propagation along the Japan trench off Tohoku: Earth, Planets and Space, v. 66, p. 1–17. doi:10.1186/1880-5981-66-135.

Bry, M., and White, N., 2007, Reappraising elastic thickness variation at oceanic trenches: Journal of Geophysical Research, v. 112, p. 582–596. doi:10.1029/2005JB004190.

Byerlee, J., 1978. Friction of rocks, Pure and Applied Geophysics, v. 116, p. 615–626.

Chen, J.Y., Morgan, J., and Jason, W., 1990, A nonlinear rheology model for mid-ocean ridge axis topography, v. 95, p. 17583-17604.

Contreras-Reyes, E., Jara, J., Maksymowicz, A., and Weinrebe, W., 2013, Sediment loading at the southern Chilean trench and its tectonic implications: Journal of Geodynamics, v. 66, p. 134–145. doi:10.1016/j.jog.2013.02.009.

Contreras-Reyes, E., and Osses, A., 2010, Lithospheric flexure modelling seaward of the Chile trench: Implications for oceanic plate weakening in the trench outer rise region: Geophysical Journal International, v. 182, p. 97–112.

Craig, T.J., Copley, A., and Jackson, J., 2014, A reassessment of outer-rise seismicity and its implications for the mechanics of oceanic lithosphere: Geophysical Journal International, v. 197, p. 63–89. doi:10.1093/gji/ggu013.

Divins, D., 2003, Total sediment thickness of the world's oceans and marginal seas, NOAA National Geophysical Data Center: Boulder, CO.

Emry, E.L., and Wiens, D.A., 2015, Incoming plate faulting in the Northern and Western Pacific and implications for subduction zone water budgets: Earth and Planetary Science Letters, v. 414, p. 176–186. doi:10.1016/j.epsl.2014.12.042.

Emry, E.L., Wiens, D.A., and Garcia-Castellanos, D., 2014, Faulting within the Pacific plate at the Mariana Trench: Implications for plate interface coupling and subduction of hydrous minerals: Journal of Geophysical Research, v. 119, p. 3076–3095. doi:10.1002/2013JB010718.

Escartin, J., Hirth, G., and Evans, B., 2001, Strength of slightly serpentinized peridotites: Implications for the tectonics of oceanic lithosphere: Geology, v. 29, p. 1023–1026. doi:10.1130/0091-7613(2001)029<1023:SOSSPI>2.0.CO;2.

Faccenda, M., Gerya, T.V., and Burlini, L., 2009, Deep slab hydration induced by bending related variations in tectonic pressure: Nature Geoscience, v. 2, p. 790–793. doi:10.1038/ngeo656.

Fujie, G., Kodaira, S., Yamashita, M., Sato, T., Takahashi, T., and Takahashi, N., 2013, Systematic changes in the incoming plate structure at the Kuril trench: Geophysical Research Letters, v. 40, p. 88–93. doi:10.1029/2012GL054340.

Garcia-Castellanos, D., Torne, M., and Fernandez, M., 2000, Slab pull effects from a flexural analysis of the Tonga and Kermadec trenches (Pacific Plate): Geophysical Journal International, v. 141, p. 479–484. doi:10.1046/j.1365-246x.2000.00096.x.

Goetze, C., 1978, The mechanisms of creep in olivine: Philosophical Transactions of the Royal Society London, v. 288, p. 99–119. doi:10.1098/rsta.1978.0008.

Goetze, C., and Evans, B., 1979, Stress and temperature in the bending lithosphere as constrained by experimental rock mechanics: Geophysical Journal of the Royal Astronomical Society, v. 59, p. 463–478. doi:10.1111/j.1365-246X.1979.tb02567.x.

Grevemeyer, I., Ranero, C.R., Flueh, E.R., Klaschen, D., and Bialas, J., 2007, Passive and active seismological study of bending-related faulting and mantle serpentinization at the Middle America trench: Earth and Planetary Science Letters, v. 258, p. 528–542. doi:10.1016/j.epsl.2007.04.013.

Hirth, G., and Kohlstedt, D., 2003, Rheology of the upper mantle and the mantle wedge: A View from The Experimentalists, Inside The Subduction Factory, 138, 83-105.

Hunter, J., and Watts, A.B., 2016, Gravity anomalies, flexure and mantle rheology seaward of circum-Pacific trenches: Geophysical Journal International, v. 207, p. 288–316. doi:10.1093/gji/ggw275.

Kirby, S.H., 1983, Rheology of the lithosphere, Reviews Of Geophysics, v. 21, p. 1458-1487.

Kuo, B.-Y., and Forsyth, D.W., 1988, Gravity anomalies of the ridge-transform system in the South Atlantic between 31° and 34.5°S: Upwelling centers and variations in crustal thickness: Marine Geophysical Research, v. 10, p. 205–232. doi:10.1007/BF00310065.

Lin, J., and Zhu, J., 2015, Global variations in gravity-derived oceanic crustal thickness and implications on oceanic crustal accretion processes, AGU Fall Meeting, Abstracts, San Francisco, p. V14A–07.

McKenzie, D.P., Jackson, J., and Priestley, K., 2005, Thermal structure of oceanic and continental lithosphere: Earth and Planetary Science Letters, v. 233, p. 337–349. doi:10.1016/j.epsl.2005.02.005.

Mei, S., Suzuki, A.M., Kohlstedt, D.L., Dixon, N.A., and Durham, W.B., 2010, Experimental constraints on the strength of the lithospheric mantle, Journal of Geophysical Research.

Müller, R.D., Sdrolias, M., Gaina, C., and Roest, W.R., 2008, Age, spreading rates, and spreading asymmetry of the world's ocean crust: Geochemistry, Geophysics, Geosystems, v. 9, p. Q04006. doi:10.1029/2007GC001743.

Naliboff, J.B., Billen, M.I., Gerya, T., and Saunders, J., 2013, Dynamics of outer-rise faulting in oceanic-continental subduction systems: Geochemistry, Geophysics, Geosystems, v. 14, p. 2310–2327. doi:10.1002/ggge.20155.

Obana, K., Fujie, G., Takahashi, T., Yamamoto, Y., Nakamura, Y., Kodaira, S., Takahashi, N., Kaneda, Y., and Shinohara, M., 2012, Normal-faulting earthquakes beneath the outer slope of the Japan trench after the 2011 Tohoku earthquake: Implications for the stress regime in the incoming Pacific plate: Geophysical Research Letters, v. 39, p. 127–137. doi:10.1029/2011GL050399.

Parker, R.L., 1973, The rapid calculation of potential anomalies: Geophysical Journal of the Royal Astronomical Society, v. 31, p. 447–455. doi:10.1111/j.1365-246X.1973.tb06513.x.

Parsons, B., and Sclater, J.G., 1977, An analysis of the variation of ocean floor bathymetry and heat flow with age: Journal of Geophysical Research, v. 82, p. 803–827. doi:10.1029/JB082i005p00803.

Ranero, C.R., Morgan, J.P., McIntosh, K., and Reichert, C., 2003, Bending-related faulting and mantle serpentinization at the Middle America trench: Nature, v. 425, p. 367–373. doi:10.1038/nature01961.

Ranero, C.R., and Sallares, V., 2004, Geophysical evidence for hydration of the crust and mantle of the Nazca plate during bending at the north Chile trench: Geology, v. 32, p. 549–552. doi:10.1130/G20379.1.

Ranero, C.R., Villaseor, A., Morgan, J.P., and Wdinrebe, W., 2005, Relationship between bending-faulting at trenches and intermediate-depth seismicity: Geochemistry, Geophysics, Geosystems, v. 6, p. Q12002. doi:10.1029/2005GC000997.

Rupke, L.H., Morgan, J.P., Hort, M., and Connolly, J.D.L., 2004, Serpentine and the subduction zone water cycle: Earth and Planetary Science Letters, v. 223, p. 17–34. doi:10.1016/j.epsl.2004.04.018.

Sandwell, D.T., Müller, R.D., Smith, W.H., Garcia, E., and Francis, R., 2014, New global marine gravity model from CryoSat-2 and Jason-1 reveals buried tectonic structure: Science, v. 346, p. 65–67. doi:10.1126/science.1258213.

Smith, W.H.F and Sandwell, D.T., 1997, Global sea floor topography from satellite altimetry and ship depth soundings: Science, v. 277, p. 1956–1962. doi:10.1126/science.277.5334.1956.

Supak, S., Bohnenstiehl, D.R., and Buck, W.R., 2006, Flexing is not stretching: an analogue study of flexure-induced fault populations, Earth and Planetary Science Letters, v. 246, p. 125–137.

Turcotte, D., and Schubert, G., 2014, Geodynamics, 3rd: New York, Cambridge University Press, 456 p.

Turcotte, D.L., McAdoo, D.C., and Caldwell, J.G., 1978, An elastic-perfectly plastic analysis of the bending of the lithosphere at a trench, Tectonophysics, v. 47, p. 193-205.

Wang, T., Lin, J., Tucholke, B., and Chen, Y.J., 2011, Crustal thickness anomalies in the North Atlantic Ocean basin from gravity analysis: Geochemistry, Geophysics, Geosystems, v. 12. doi:10.1029/2010GC003402.

Watts, A.B., 2001, Isostasy and flexure of the lithosphere: New York, Cambridge University Press, 458 p.

Yamano, M., and Uyeda, S., 1990, Heat-flow studies in the Peru Trench sub-duction zone, in Suess, E., von Huene, R., et al., eds., Proceedings of the Ocean Drilling Program, Scientific Results, College Station, TX: Ocean Drilling Program, p. 653–661.

Zhang, F., Lin, J., and Zhan, W., 2014, Variations in oceanic plate bending along the Mariana trench: Earth and Planetary Science Letters, v. 401, p. 206–214. doi:10.1016/j.epsl.2014.05.032.

Zhang, F., Lin, J., Zhou, Z., Yang, H., and Zhan, W., 2018a, Intra- and inter-trench variations in flexural bending of the Manila, Mariana and global trenches: Implications on plate weakening in controlling trench dynamics: Geophysical Journal International, v. 212, p. 1419–1449. doi:10.1093/gji/ggx488.

Zhang, J., Sun, Z., Xu, M., Yang, H.F., Zhang, Y.F., and Li, F.C., 2018b, Lithospheric 3-D flexural modelling of subducted oceanic plate with variable effective elastic thickness along Manila Trench: Geophysical Journal International, v. 215, p. 2071–2092. doi:10.1093/gji/ggy393.

Zhang, J., Xu, M., and Sun, Z., 2018c, Lithospheric flexural modeling of the seaward and trenchward of the subducting oceanic plates: International Geology Review, p. 1–16. doi:10.1080/00206814.2018.1550729.

Zhou, Z., and Lin, J., 2018, Elasto-plastic deformation and plate weakening due to normal faulting in the subducting plate along the Mariana Trench: Tectonophysics, v. 734–735, p. 59–68. doi:10.1016/j.tecto.2018.04.008.

Zhou, Z., Lin, J., Behn, M.D., and Olive, J.-A., 2015, Mechanism for normal faulting in the subducting plate at the Mariana Trench: Geophysical Research Letters, v. 42, p. 4309–4317. doi:10.1002/2015GL063917.

Zhou, Z., Lin, J., and Zhang, F., 2018, Modeling of normal faulting in the subducting plates of the Tonga, Japan, Izu-Bonin, and Mariana trenches: Implications for near-trench plate weakening: Acta Oceanologica Sinica, v. 11, p. 53–60. doi:10.1007/s13131-018-1146-z.

Appendices

Appendix A. Methods of modelling flexural bending profiles

1. Calculation of 'Non-airy-isostatic' topography

To better reveal the flexural bending of a subducting plate, we first calculate 'non-isostatic' topography by removing the following predictable components from the observed bathymetry: (1) Sediment loading; (2) Airy-isostatic topography calculated from gravity-derived crustal thickness model; and (3) Age-related thermal subsidence. The resultant 'non-isostatic topography' should reflect stress-supported flexural bending, as well as deviations from the above reference models (Zhang *et al*. 2014, 2018a), enabling us to better investigate near-trench flexural bending of a subducting plate.

a) Bathymetry and sediment thickness. The seafloor bathymetry data of the investigated trenches are extracted from the global marine bathymetry database (Smith and Sandwell 1997; http://topex.ucsd.edu/WWW_html/mar_topo.html, v18.1) with data grid spacing of 0.25 min. The sediment thickness data are extracted from the global sediment database (Divins 2003) of the National Geophysical Data Centre (NGDC) with grid spacing of 5 min.

b) Gravity-derived crustal thickness. The gravity-derived crustal thickness is calculated by the following steps. (1) *Mantle Bouguer gravity anomaly*: We first extract free-air anomaly (FAA) from the global database of Sandwell *et al*. (2014; http://topex.ucsd.edu/grav_outreach/index.html) with 1-min grid spacing. We then calculate mantle Bouguer anomaly (MBA) by removing from FAA the gravitational effects of seawater–sediment, sediment–crust, and crust–mantle interfaces, assuming a reference crustal thickness model of 6 km. (2) *Thermal correction*: We calculate 3D mantle temperature field of a 100-km-thick mantle layer by assuming 1D vertical cooling (Turcotte and Schubert 2014), using the plate age data of Müller *et al*. (2008). The top and bottom temperatures of the mantle layer are assumed to be T_t= 0°C and T_m = 1,350°C, respectively. We then convert the thermal structure into a 3D grid by $\Delta\rho = -\alpha\rho_0(T - T_0)$, where T_0 = 1,350°C and ρ_0= 3.3 × 10^3 kg/m^3 are reference values of mantle temperature and density, respectively, and α= 3 × 10^{-5}/K is thermal expansion coefficient. (3) *Residual mantle Bouguer anomaly (RMBA)*: We then remove the calculated gravitational effects of the lithospheric cooling from the MBA to obtain the residual mantle Bouguer anomaly (RMBA). (4) *Crustal thickness model*: Finally, we calculate a reference crustal thickness model by downward continuation of the RMBA signals to a constant reference depth of 6 km (Parker 1973; Kuo and Forsyth 1988; Wang *et al*. 2011; Lin and Zhu 2015).

c) Isostatic topography. For topographic features that can be approximately described by local Airy isostasy, e.g. ridges and seamounts with roots, we use the local Airy isostasy model to calculate the expected topography arising from thickened crust (Zhang *et al*. 2014). The Airy-isostatic topography is calculated by the following equation: $T_{iso} = (H_c - \overline{H_c}) \times \frac{(\rho_m - \rho_c)}{(\rho_m - \rho_w)}$, where H_c is gravity-derived crustal thickness, $\overline{H_c}$is a reference crustal thickness of 6 km,ρ_w= 1.03 × 10^3 kg/m^3,ρ_c= 2.7 × 10^3 kg/m^3, andρ_m= 3.3ρ_s10^3 kg/m^3 are assumed densities of seawater, crust, and mantle, respectively. The constant parameters used in this study are listed in Table 1.

d) Non-isostatic topography. We calculate non-Airy-isostatic topography of the study region by removing the sediment loading, Airy-isostatic topography, and thermal subsidence from bathymetry using methods of Zhang *et al*. (2014). Our analysis reveal that the non-Airy-isostatic topography, which is called non-isostatic topography hereafter, and free-air anomaly show similar overall spatial variations (Figure B5), although the FAA contains slightly less information due to upward attenuation of the gravity signal. Thus, we use the non-isostatic topography as a primary indicator for flexural deformation caused by plate bending (e.g. Zhang *et al*. 2014, 2018a), while using the FAA (Figure B5) as complementary constraints (Hunter and Watts 2016).

2. Inversion of bending parameters

For 73 profile sections of the global trenches (Figure 1) and five sections of deepest points (Figure B1), we use finite-difference methods (Contreras-Reyes and Osses 2010; Zhang *et al*. 2014) to model the flexure parameters of the subducting plates. The models assume an elastic plate of variable effective elastic thickness on top of a non-viscous asthenospheric half-space. The effective elastic plate thickness is assumed to be reduced from a maximum value of $T_e{}^M$ (seaward of the outer-rise) to a minimum value $T_e{}^m$ (trench-ward of outer-rise) at a breaking point distance x_r near the outer-rise. We obtain five best-fitting parameters (Table B1) that control the bending shape of each section: Axial vertical loading (-V_0) and bending moment (-M_0), maximum ($T_e{}^M$) and minimum ($T_e{}^m$) effective elastic thickness, as well as break point (x_r) by solving the following equations (Turcotte and Schubert 2014):

$$-\frac{d^2M(x)}{dx^2} + \frac{d}{dx}\left[F(x)\frac{dw(x)}{dx}\right] + \Delta\rho g w(x) = q(x), \qquad (1)$$

where *M(x)* is bending moment, *F(x)* is horizontal force, $\Delta\rho g w(x)$ = (ρ_m-ρ_w)$gw(x)$ is restoring force, and *q(x)* is vertical sediment loading. The bending moment is calculated by:

$$M(x) = -D(x)\frac{d^2w(x)}{dx^2}, \qquad (2)$$

where flexural rigidity can be calculated by $D(x) = \frac{ET_e^3(x)}{12(1-v^2)}$, *E* is Young's modulus, *v* is Poisson's ratio, and *T*$_e$*(x)* is effective elastic thickness. The vertical loading *V(x)* is:

$$V(x) = \frac{dM(x)}{dx} - F(x)\frac{dw(x)}{dx}, \qquad (3)$$

where the horizontal force *F(x)* is assumed to be relatively small and therefore both the flexural height *w(x)* and flexural deflection *dw(x)/dx* approach zero at a great distance from the trench axis.

Boundary conditions and other assumptions for material properties, as well as technical details, are the same as in Zhang *et al*. (2014); (2018a). The best-fitting parameters (Table B1) are obtained through inversions that minimize the root-mean-square (RMS) misfits between the interpreted bending deformation and the theoretical prediction from the bending models.

Appendix B. Flexural parameters of 15 global trenches and five deepest regions

This section describes the results of the flexural bending parameters calculated for the 15 global trenches (Table B1) and five deepest regions (Table B2). In Table B1, the averaged values of a parameter from multiple profiles for a study region is shown on the top, while maximum and minimum values of the same parameter among the individual profiles are shown on the bottom.

Table B1. Best-fitting bending parameters for 15 global trenches for trench-averaged values (top column) and range (bottom column) among individual profiles.

Trench Name	$-V_0$ (10^{12} N/m)	$-M_0$ (10^{16} N)	T_e^M (km)	T_e^m (km)	X_r (km)	$S_\Delta T_e$ (km^2)
M. America	0.21	3.6	34	13	36	781
	0.0–0.4	2-5	32-35	10-16	20-40	462-912
Peru	0.34	6.0	40	21	54	995
	0.0–1.0	2-11	33-44	17-24	40-65	873-1268
Chile	0.57	8.3	42	20	60	1308
	0.1–1.2	4-17	25-45	15-25	45-80	396-1890
W. Aleutian	−0.07	14.9	47	26	86	1770
	−0.5-0.5	8-22	44-50	20-32	50-105	1188-2475
E. Aleutian	−0.40	11.2	46	24	58	1251
	−0.7-0.0	6-14	40-50	18-28	45-70	880-1500
Sumatra	−0.08	8.0	51	24	38	1070
	−0.4-0.4	5-13	47-55	21-32	10-65	172-1528
N. Philippine	0.00	5.0	44	20	45	1089
	0.0–0.0	5-5	44-44	20-20	45-45	1089-1089
S. Philippine	−0.20	12.0	47	21	43	1086
	−0.6-0.2	8-18	40-50	16-25	40-45	960-1200
Tonga	1.26	8.6	47	19	55	1517
	0.9–1.7	4-13	43-50	15-23	45-60	1296-1764
Kermadec	1.30	6.8	49	19	73	2163
	0.8–1.7	2-12	46-50	16-22	60-80	1800-2600
Kuril	0.77	12.8	45	24	76	1616
	0.0–1.5	4-21	39-50	20-29	60-85	1155-2125
Japan	0.25	16.0	50	31	83	1546
	0.1–0.4	14-18	48-52	31-31	80-85	1428-1664
Izu-Bonin	1.77	19.3	53	32	98	2084
	1.1–2.2	18-22	51-54	31-32	95-100	2040-2160
S. Mariana	0.63	13.3	52	30	82	1917
	0.4–1.1	9-18	48-55	28-32	55-100	1056-2750
N. Mariana	0.73	16.8	50	26	70	1556
	0.4–1.3	10-22	46-55	22-32	40-110	1080-2424

Table B2. Region-averaged bending parameters for the five deepest regions.

Deep Name	$-V_0$ (10^{12} N/m)	$-M_0$ (10^{16} N)	T_e^M (km)	T_e^m (km)	X_r (km)	$S_\Delta T_e$ (km^2)
Challenger	2.6	6	51	20	85	2295
Horizon	1.5	10	42	10	60	1386
Sirena	2.6	6	51	23	100	2810
Galathea	1.2	11	45	12	65	1463
Scholl	1.7	1	42	13	75	2205

Table B3. Parameters for the mantle flow laws used in this study.

Parameters	Description	Value
B	Pre-exponential coefficient (s^{-1} MPa^{-n})	1.1×10^5
n	Stress exponent for power-law creep flow	3.5
E	Activation energy (kJ mol^{-1})	530
V	Activation volume (10^{-6} m^3 mol^{-1})	14
A	Pre-exponential coefficient (s^{-1} MPa^{-m})	1.4×10^{-7}
n	Stress exponent for low-temperature plasticity flow	2
$H_\square$	Zero-stress activation enthalpy (kJ mol^{-1})	320
σ_p	Peierls stress (GPa)	5.9
p	Geometry-depedent exponent	0.5
q	Geometry-depedent exponent	1

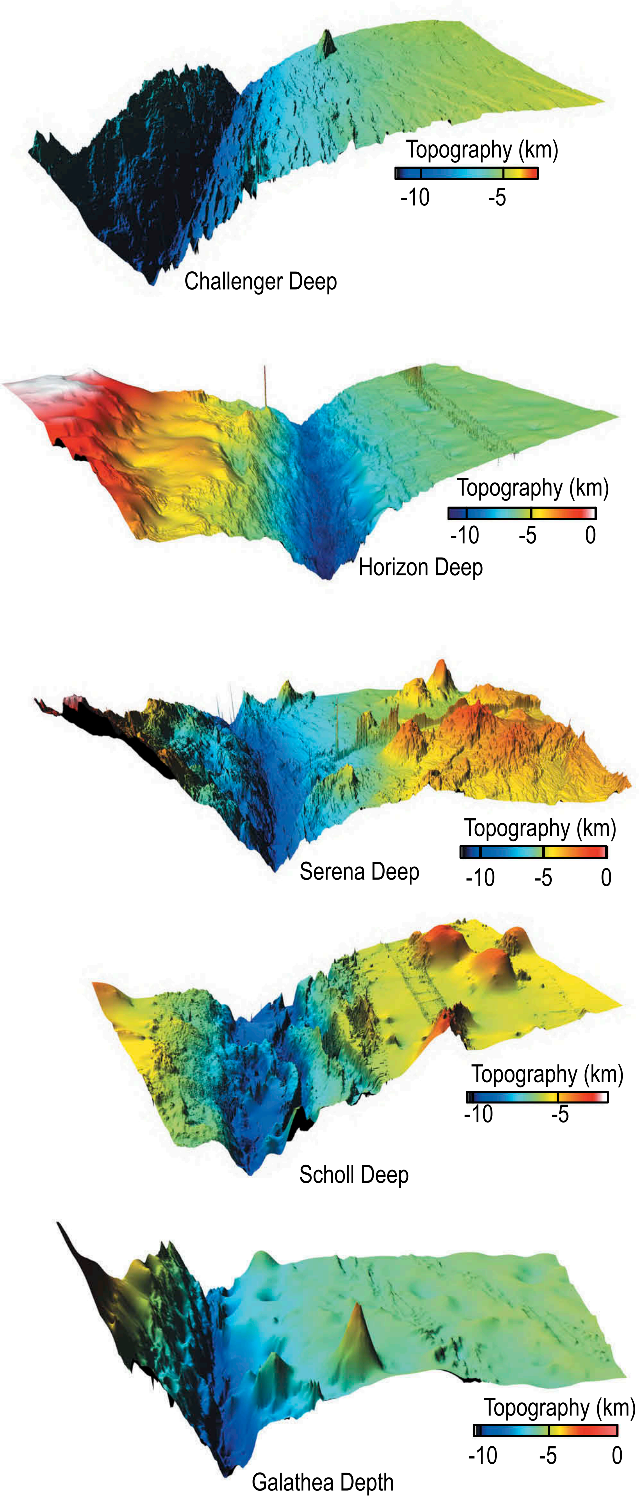

Figure B1. 3D topography of the Challenger, Horizon, Serena, and Scholl Deeps, and Galathea Depth.

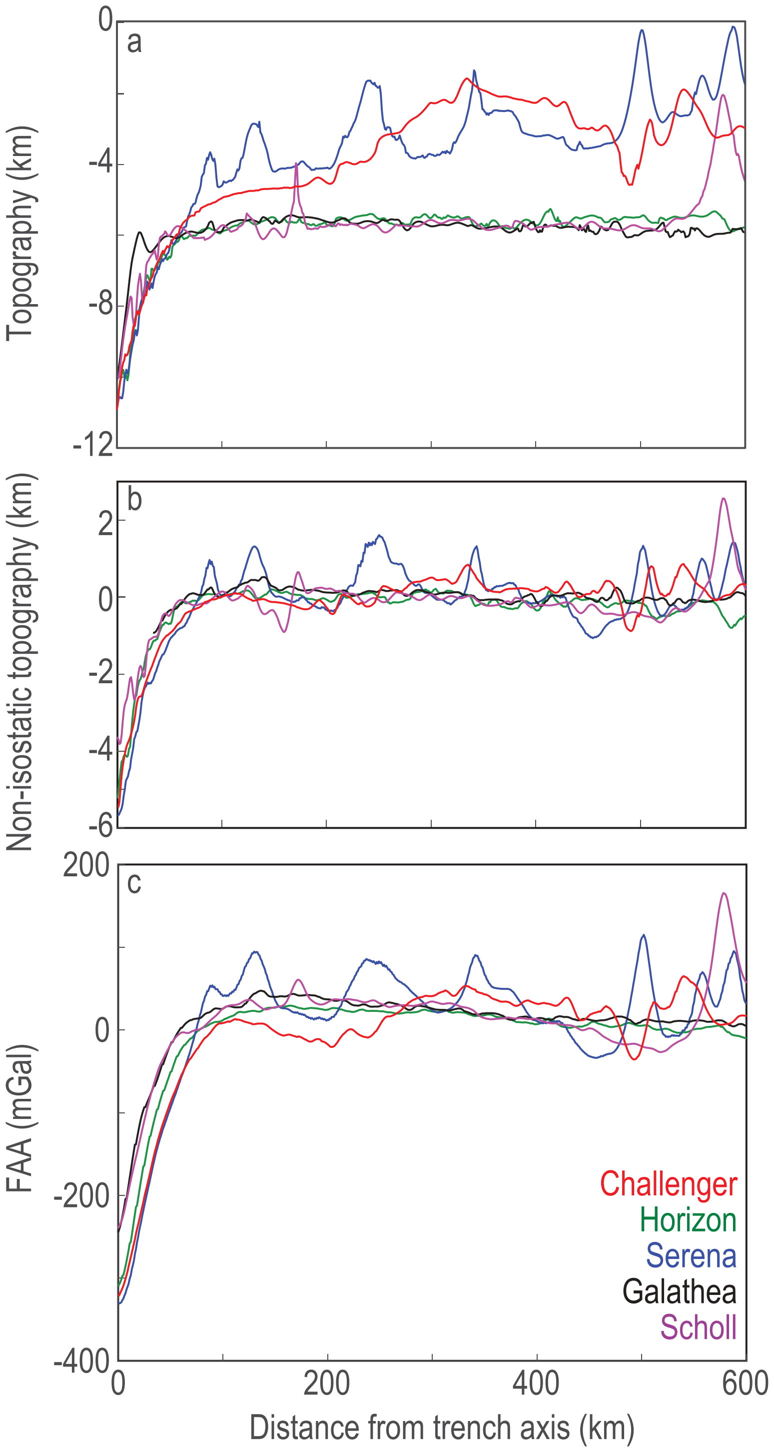

Figure B2. Topography (a), non-isostatic topography (b), and free-air anomaly (c) of the Challenger, Horizon, Serena, and Scholl Deeps, and Galathea Depth.

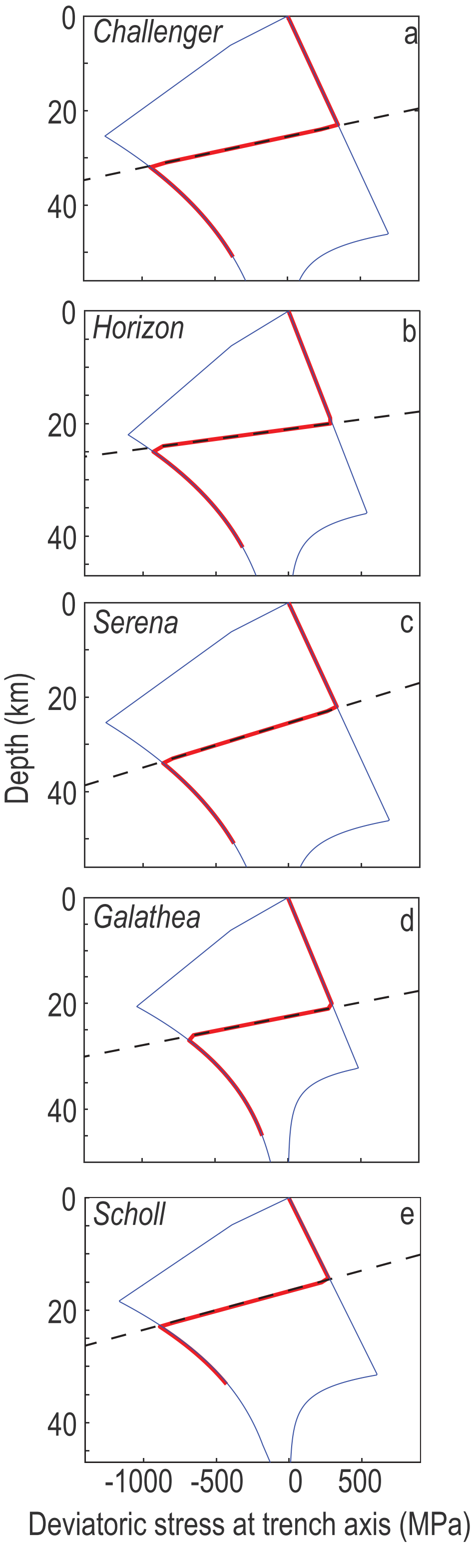

Figure B3. Calculated deviatoric stresses (a–e) of the Challenger, Horizon, Serena, and Scholl Deeps, and Galathea Depth. Blue curves show the yield strength envelope (YSE), black-dashed lines mark the slope of the elastic core, and red curves mark the deviatoric stresses as a function of depth in the plate.

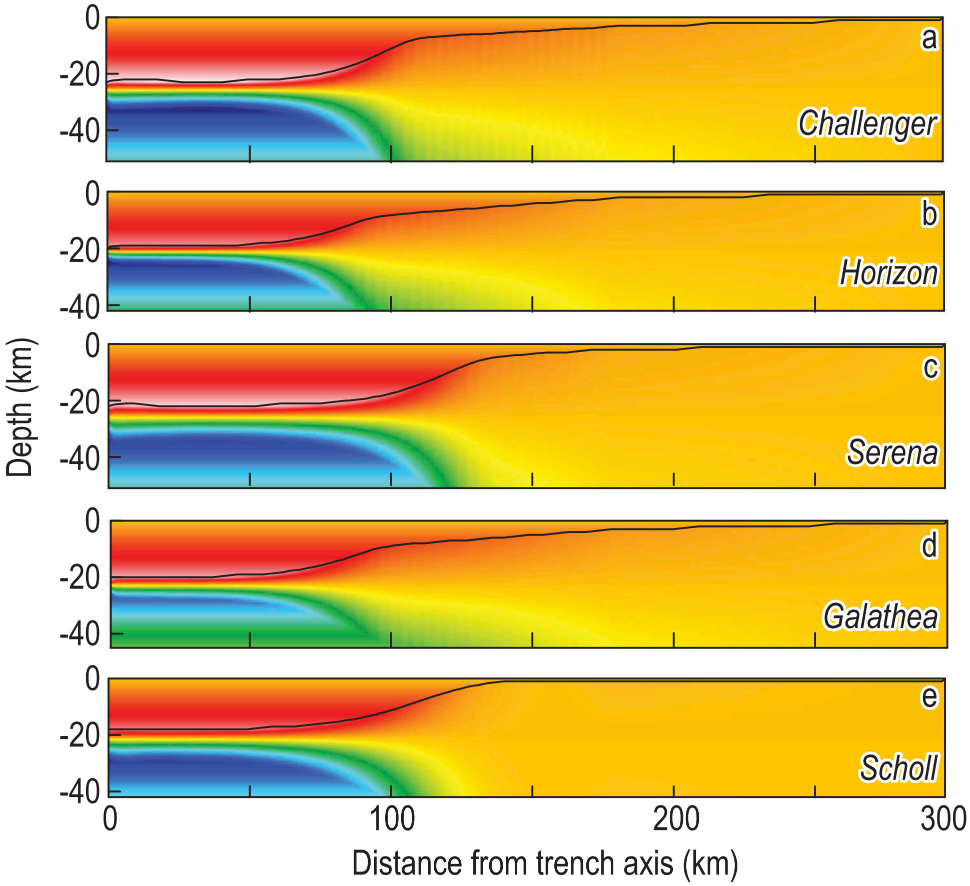

Figure B4. Calculated deviatoric stresses in the subducting plates of the Challenger, Horizon, Serena, and Scholl Deeps, and Galathea Depth. Black curves mark the maximum yield zone depth.

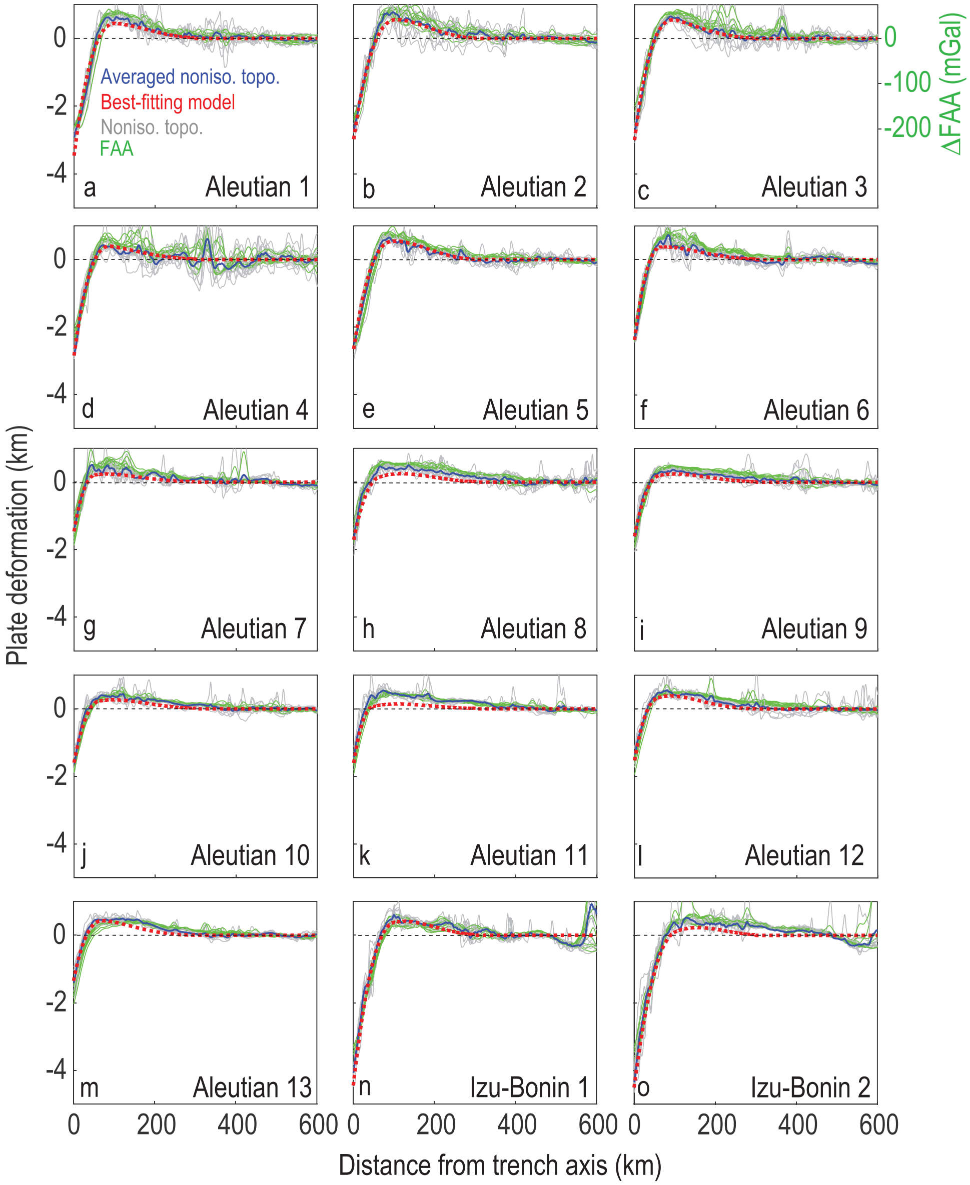

Figure B5. Calculated and modelled plate deflection of an array of global trenches. Shown are the calculated non-isostatic topography of individual profiles (thin grey), mean profiles of non-isostatic topography for each group (thick blue), and the magnitude of variation in free-air gravity anomalies (FAA, thin green). Red dashed curves indicate modelled bending shapes for each group.

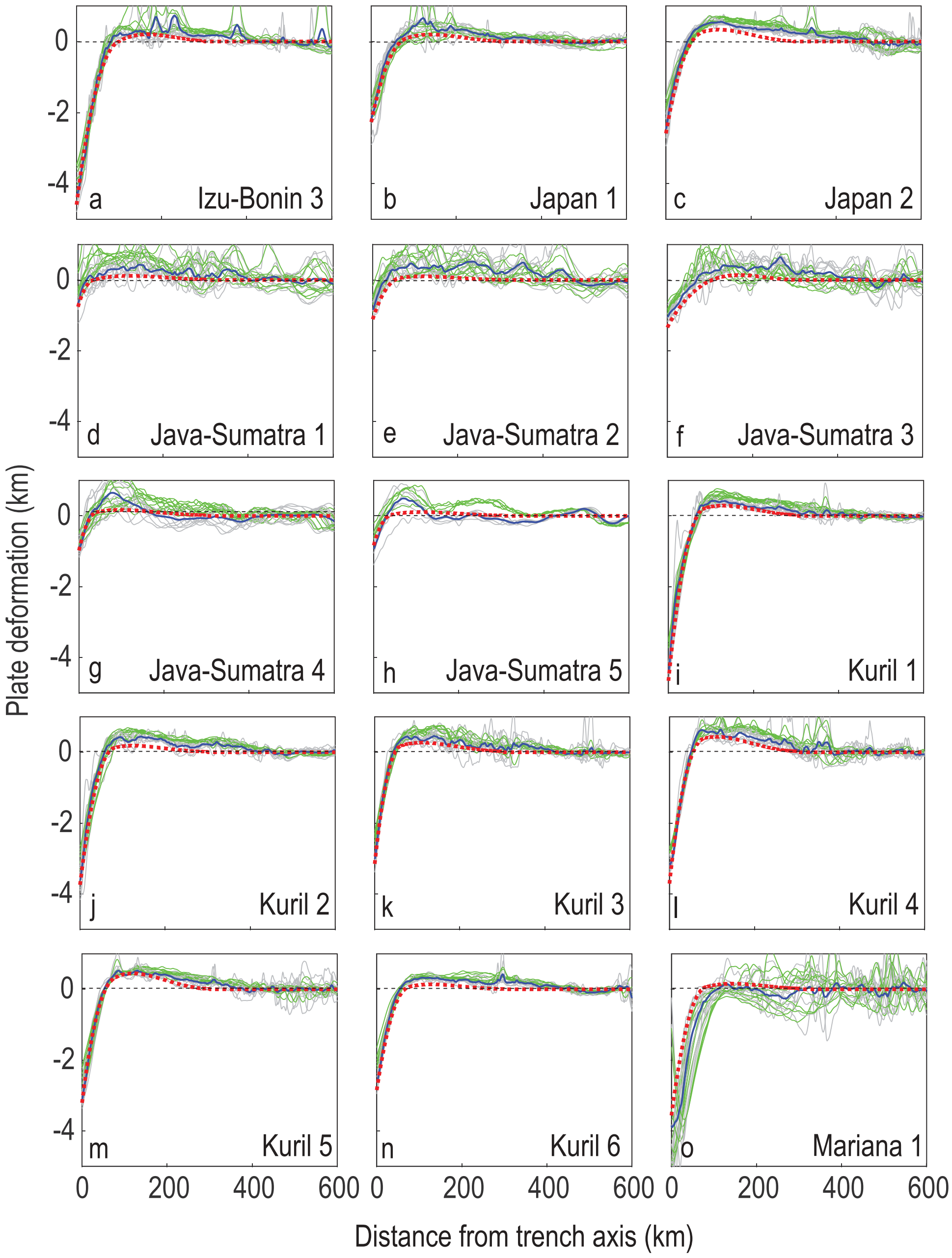

Figure B5. Continued.

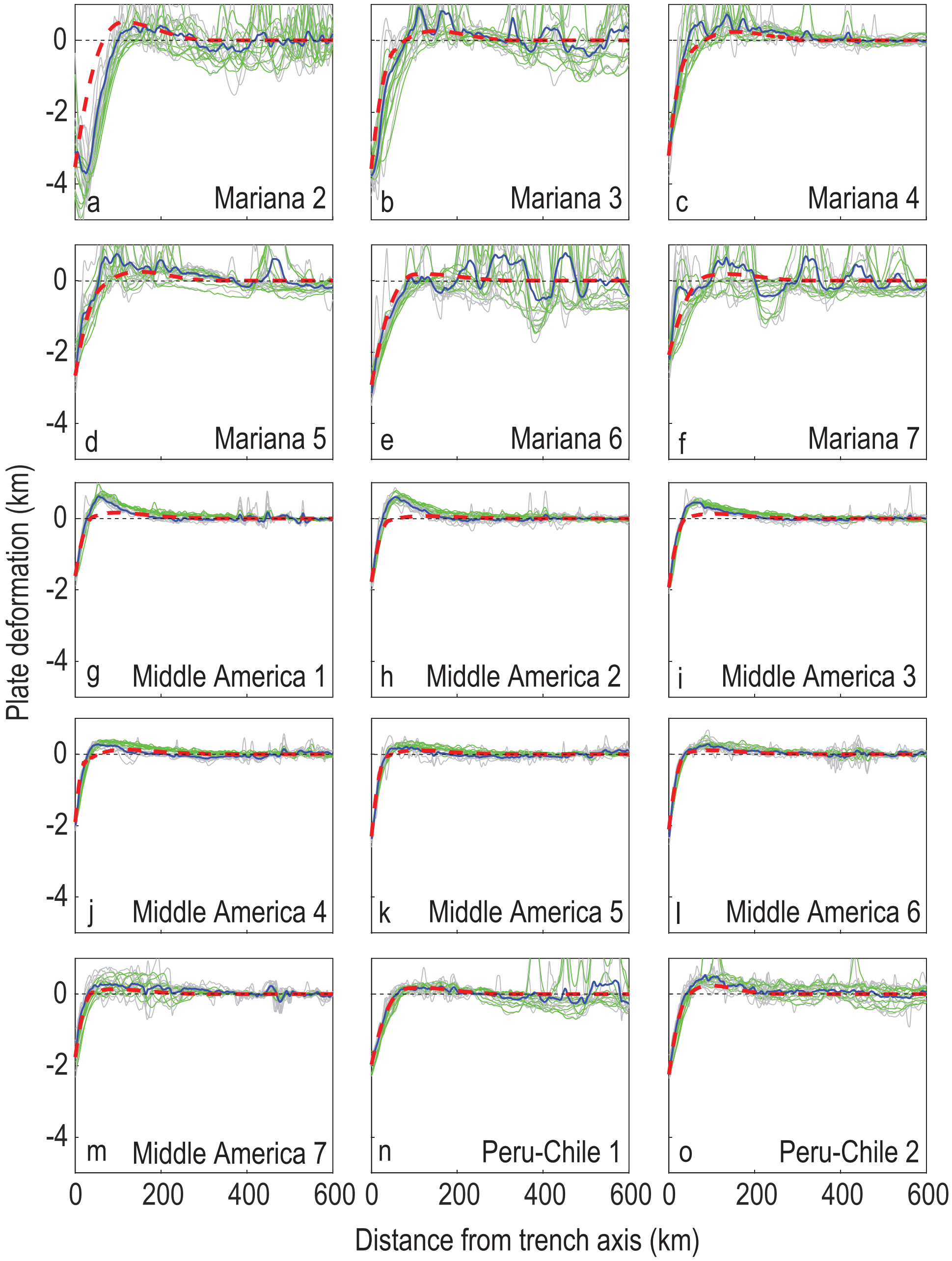

Figure B5. Continued.

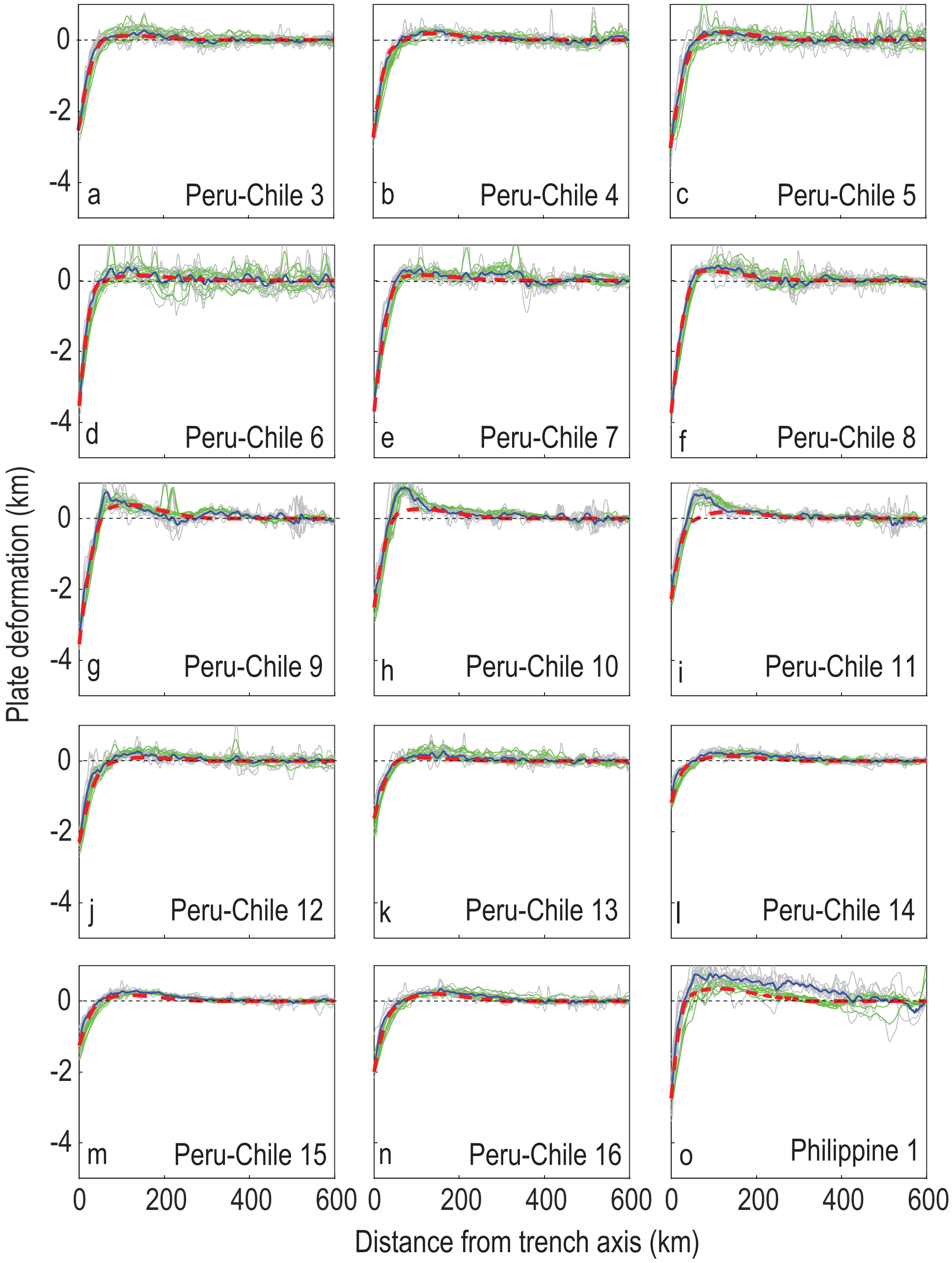

Figure B5. Continued.

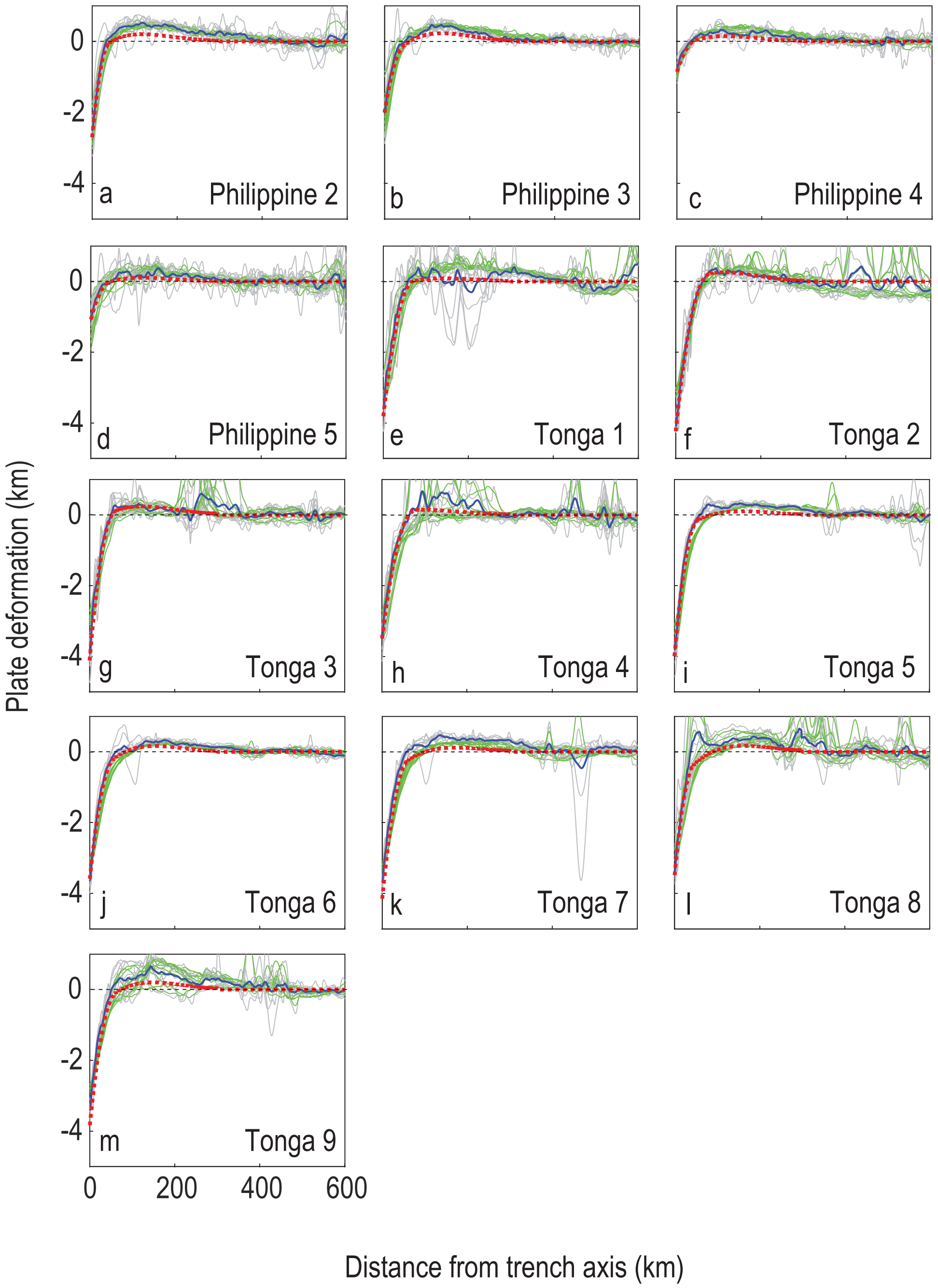

Figure B5. Continued.

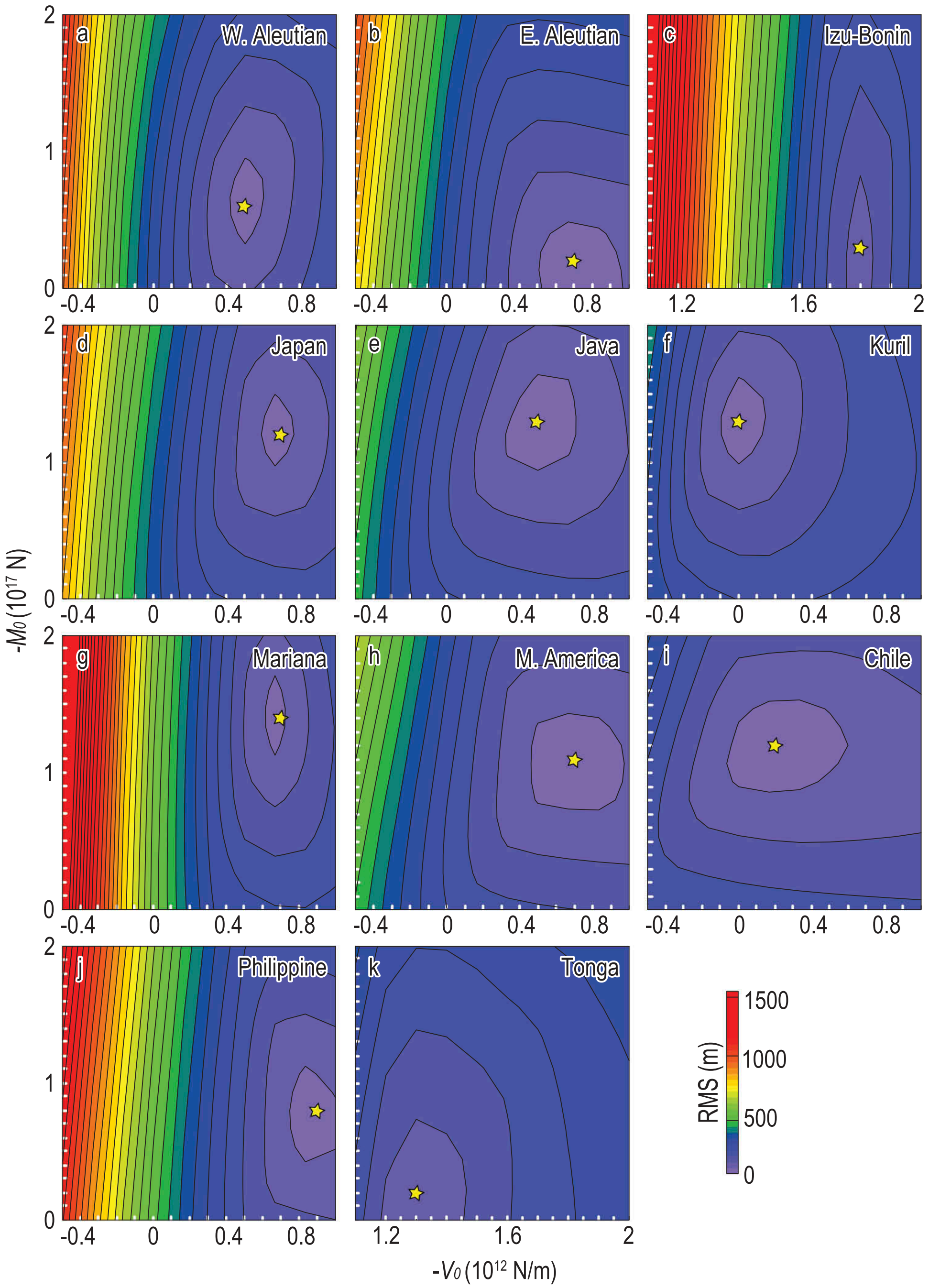

Figure B6. Root mean square (RMS) difference between interpreted plate deformation and modelled flexural bending shapes as functions of model vertical loading V_0 and bending moment M_0. Yellow stars are the best-fitting solutions with minimum RMS. Parameter grids of V_0 and M_0 used in the searching minimum RMS solutions are shown by white ticks in the horizontal and vertical axes.

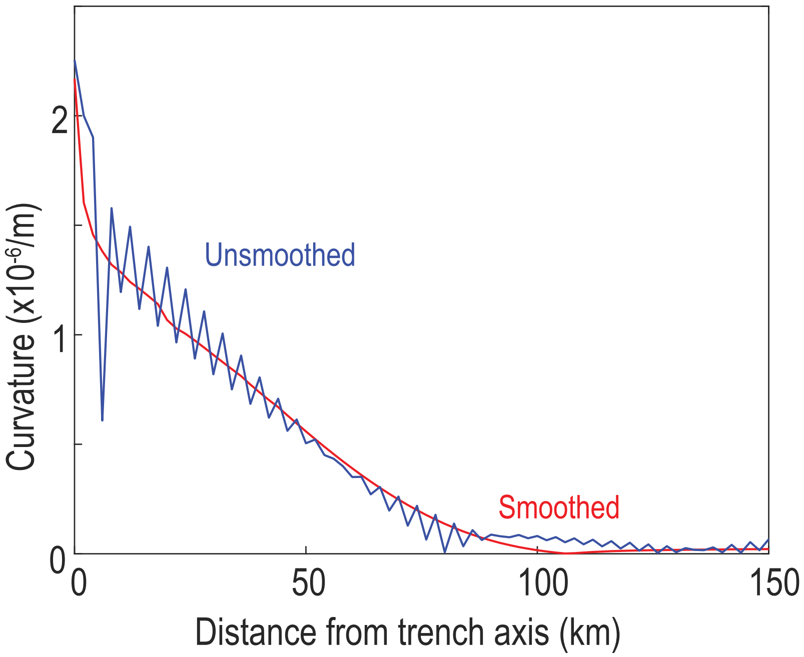

Figure B7. An example showing the comparison of calculated plate curvature with (red) and without (blue) smoothing short-wavelength numerical undulations in a profile.